Investigating the connection between optical and very high energy gamma-ray emission of BL Lac objects

Master's thesis
University of Turku
Astronomy
2023
B.Sc. Jan Aaltonen
Examiners:
Dr. Elina Lindfors
Prof. Seppo Mattila

The originality of this thesis has been checked in accordance with the University of Turku quality assurance system using Turnitin Originality Check service.

UNIVERSITY OF TURKU
Department of Physics and Astronomy

Aaltonen, Jan Investigating the connection between optical and very high energy gamma-ray emission of BL Lac objects

Master's thesis, 67 pp.
Astronomy
2023

In this thesis, I have performed systematic comparison of the occurrence of optical and very high-energy (VHE) gamma-ray high states in BL Lac objects (BL Lacs). BL Lacs are the most numerous extragalactic VHE gamma-ray sources. They emit electromagnetic radiation from radio to VHE gamma-ray band and this emission is extremely variable, timescales ranging from years to days to hours.

Optical emission is synchrotron emission, and VHE gamma-rays are inverse Compton emission. The VHE emission mechanism is either synchrotron self-Compton process (SSC) or external Compton process (EC) but both predict a connection between optical and gamma-ray flares. Also, several mechanisms may affect the time-lags between optical and gamma-ray flares but it is impossible to predict them accurately. Optical to VHE gamma-ray connection should also be affected by the synchrotron peak frequency of the source since higher peak frequency in the X-ray band leads to the variability in the optical domain to be in some cases very small and the synchrotron flares have the best visibility in the X-ray range as is seen for blazars Mrk 421 and Mrk 501, for example.

A correlation between the two bands would hint a common origin for both VHE and optical emission. To find the correlation I first try to characterize the optical variability timescales to understand in which time windows I should compare the optical and VHE gamma-ray fluxes. To determine the optical flares from the light curves, I used a statistical method called Bayesian blocks along with hill-climbing algorithm. After this I checked if these flares have a common duration. The flare durations were distributed rather uniformly, but the distribution peaked around 14 days, which we used as a minimum window when comparing the fluxes.

In VHE gamma-ray band the data is very sparse for most of the BL Lac objects and can consist only of one to few observations. We defined uniform criteria on how to define high and low states in VHE gamma-ray band and applied it to all objects, also to those few that had several years of data. I analyzed how well the high states coincide within the two bands. I calculated the average optical fluxes for each light curve and within each VHE observation window. The result was that on average the optical flux within high VHE flux state windows is higher than the average optical flux. This result was investigated further, and by simulating light curves we could find out the chance probability of this occurring in a repetition of simulated data. The result was that the chance probability is very low for the high state sample.

The findings of this thesis are in line with previous studies with much smaller samples. Even if the sample of this thesis is significantly larger, further observations in VHE gamma-ray band are needed to remove the observational biases from our sample. Furthermore, real correlation studies between optical and VHE gamma-ray band would be needed, as more VHE gamma-ray light curves will become available.

Keywords: active galactic nuclei, blazar, BL Lacertae object, optical flares, very high-energy gamma-ray emission

Contents

1 Introduction

The central region of galaxies can be powered by active accretion to supermassive black holes (SMBHs) and these active regions are called active galactic nuclei (AGN) [1, 2]. A galaxy that host an AGN is called an active galaxy. AGN are one of the most luminous and energetic phenomena detectable to high redshifts in the Universe. The differences between active galaxies and nonactive galaxies are numerous but the division is not always evident. AGN have high luminosity, broad-band continuum emission, strong emission lines and flux variability on time scales of minutes to years [3–9]. A small number of AGN also have relativistic jets that shoot out from the poles of the central engine. However, some AGN do not have all of these features but they are still categorized as AGN. All galaxies host a SMBH in their nucleus but the SMBH is not always accreting and when it is the activity has different phases. This leads to many different categories of AGN that help us classify and identify these objects [10].

Figure 1 represents the structure of a typical AGN [11]. The picture is not on scale. In the middle, there is the SMBH in which matter is funneled to from the accretion disk surrounding the SMBH. This disk consisting of plasma has a broad line region (BLR) around it where the broad and optical/UV lines are produced. The inner radius of this region scales with luminosity and is $\sim$ 10–100 light days according to reverberation mapping studies for example by Kaspi et al. (2005) [12]. Reverberation mapping is a technique that is used to measure light-travel-time delay over which broad emission line flux responds to continuum luminosity variations and to thus determine the characteristic size of the BLR around the photoionizing central object, which in this case is the accretion disk. The size and the line width of the BLR give an estimate of the mass of the SMBH by assuming that the emission lines are broadened largely by the virial gas motions in the gravitational potential of the SMBH. Surrounding the BLR we have a dust obscuring torus, and it blocks

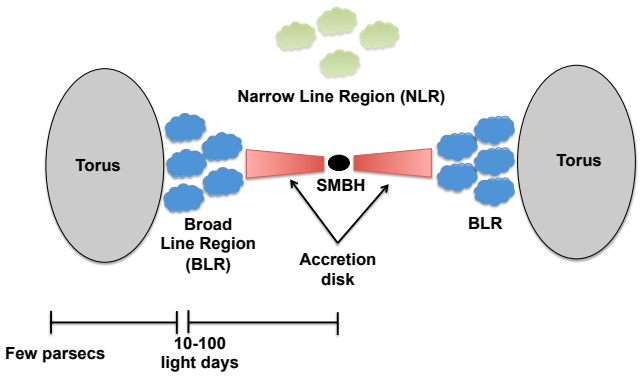

Figure 1: The structure of a typical AGN. [11]

the view to the nucleus of AGN that is viewed from the edges [13]. The torus is molecular and located within few parsecs from the SMBH [11]. The inner radius of the torus also scales with luminosity which is shown by near-infrared reverberation studies [14]. There is also a narrow line region (NLR) located at $\sim$ 100–300 pc from the SMBH, where the narrow optical lines are created [11]. The Figure shows the radio-quiet case where radio jets are not seen. In radio-loud case these jets are launched from the proximity of the poles of the SMBH [10]. The different features that are observed in different types of AGN depend on their alignment as well as the intrinsic properties of the AGN themselves, according to the unification model of AGN.

1.1 Broad-band emission

Spectral energy distribution (SED) is used to characterize astronomical objects. It shows how the energy changes with frequency or wavelength: for AGN the observed SED includes frequencies of the whole electromagnetic spectrum all the way from radio emission to high-energy (HE) or even to very-high-energy (VHE) gamma-ray

band. In normal galaxies, the SED has only frequencies from the thermal spectrum radiated by the stars as well as some from dust that re-emits the starlight again in the far-infrared (far-IR) region. The nucleus of an AGN has different parts that can produce emission by both thermal and non-thermal processes in AGN. The different emission components that are seen from different types of AGN are synchrotron emission from the jet, inverse-Compton (IC) emission from the jet, blackbody emission from the accretion disk, blackbody emission from the host galaxy and blackbody emission from heated dust. [10]

Synchrotron radiation is generated by the electrons in magnetic fields of jets; thus, it is observed in some AGN in radio band. These AGN are called radio-loud AGN [15, 16]. When this is not observed, the AGN is said to be radio-quiet. The host galaxy adds to the thermal emission of the spectrum in normal galaxies as well as in AGN in far-IR, optical and UV bands [10]. In addition, in AGN the accretion disk and the dusty torus produce thermal emission which can be observed in far-IR, optical and UV. The accretion disk is surrounded by a hot corona where lower energy UV photons produced by the disk are scattered to higher energies and this is thought to be the origin of the X-ray spectrum observed in AGN.

The high energy X-ray emission up to very high energy emission could be caused by inverse-Compton (IC) mechanisms by non-thermal synchrotron electrons in radio-loud AGN [10]. In this case the jet would be essentially made of leptons. This is called the leptonic model and it would ensue from the scattering of low energy photons from the jet as in synchrotron self-Compton process (SCC) or of photons that are not originated from the jet, which is called the external Compton process (EC). There is also the hadronic model in which the non-thermal radiation is produced by ultrarelativistic protons and their secondary particle cascades. Figure 2 is the spectral energy distribution of 3C 273, where parabolas represent the different components of emission. Synchrotron radiation component from the jet is in red, IC

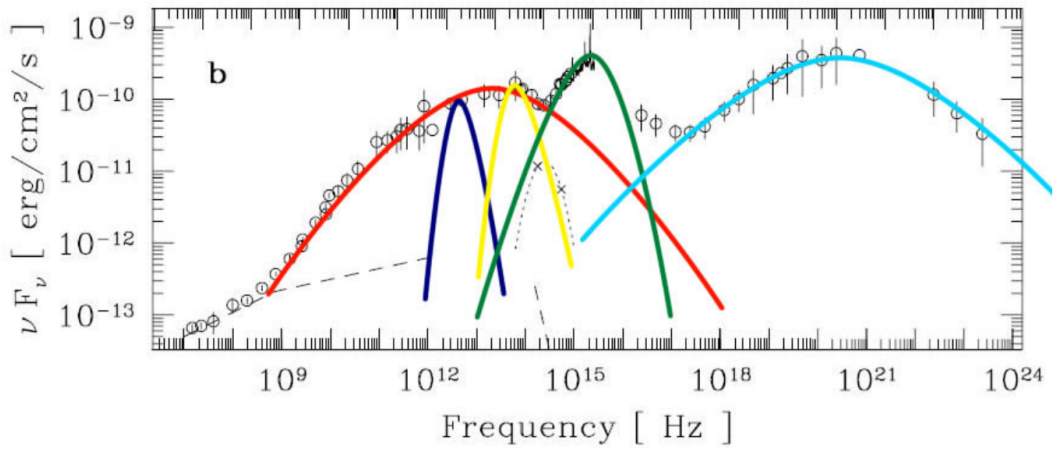

Figure 2: Spectral energy distribution of 3C 273. The different emission components are visualized with parabolas: synchrotron radiation component from the jet is in red, IC radiation component from the jet is in light blue, blackbody radiation component from the host galaxy is in yellow and blackbody radiation component from heated dust in dark blue. [17]

radiation component from the jet is in light blue, blackbody radiation component from the host galaxy is in yellow and blackbody radiation component from heated dust in dark blue.

1.2 Blazars

Blazars are a type of AGN that have a powerful jet, the alignment of which is close to our line of sight [13]. Since the jet speeds are also relativistic, the radiation produced by the jet that is moving towards us, the viewer, is Doppler boosted, and the radiation produced by the jet that is moving away from us is stagnated. Blazars are luminous and can be detected over all frequencies in the electromagnetic spectrum. They are radio-loud objects so they emit synchrotron radiation and are highly variable as well as strongly polarized in radio and optical bands [18].

Blazars are categorized in two main classes based on how strong emission lines are present in their optical spectra: BL Lacertae objects (BL Lacs) possess either no emission lines or very weak emission lines and flat-spectrum radio quasars (FSRQs) have luminous broad emission lines. We do not see emission lines in BL Lacs due

to either the emission from the jet outshining the emission from the clouds in the BLR or the lines being intrinsically weak. [19]

It is thought that this division is due to different parent populations: the parent population of BL Lacs is thought to be Fanaroff-Riley type I (FR I) [20] and the population of FSRQs is thought to be FR II [21, 22]. Observations have, however, proven that this is not always the case. This is due to radio galaxies being either FR Is or FR IIs, and that the large-scale radio jets of these types have very different appearances. Additionally, BL Lacs are divided into three subclasses based on the peak frequency of their synchrotron emission in their SEDs: low peaking BL Lacs (LBLs), intermediate peaking BL Lacs (IBLs) and high peaking BL Lacs (HBLs) [23]. Classifying these objects is not always straightforward because of the variability of the emission. For example the famous BL Lacertae does not show any spectral lines when it is in its flaring state but in its low state it might show some lines. [13, 24–28]

VHE gamma-ray blazars that are the topic of this thesis are dominantly BL Lacs. FSRQs and BL Lacs can show rather different variability patterns and therefore in this thesis work we only concentrate on BL Lacs.

1.3 Jets

Jets are collimated outflows associated with many types of high-energy astronomical objects but in this thesis work I only discuss jets found in radio-loud AGN, ejected near the poles of the central supermassive black hole. Energy, momentum and angular momentum are being carried away from the center to large distances by the jets. It is still not completely known what is their composition and how they are being generated as well as what keeps them collimated. However, theoretical models of jets point to the magnetic field extracting energy from the black hole or the accretion disk as the origin that triggers the jet. Jets can be divided into small,

parsec-scale jets and massive, large-scale jets extending over several kiloparsecs. [29]

Parsec-scale jets appear one-sided due to Doppler boosting or relativistic beaming that occurs due to the jet geometry and relativistic nature of the jet beam [29–31]. The jet that moves away from us is stagnated beyond the limits of observations but the jet that moves towards us, i.e. is closer to the direction of our line of sight is boosted and appears brighter. To uncover their structure, very high angular resolutions are needed due to them being only a few parsecs away from the nucleus. This is achieved in the radio and millimeter bands using Very Long Baseline Interferometry (VLBI) in which radio telescopes around the world simultaneously observe the same targets and form an interferometer with an angular resolution determined by the distance between the telescopes and the observing frequency [32].

The jets are observed within a $\lesssim 10^{\circ}$ angle along our line of sight [33]. Because of the small viewing angle and relativistic speeds, superluminal motion or motion that appear to be faster than the speed of light is observed: velocities up to 50 c have been observed [34]. This effect affects the brightness as well making the variations in brightness in blazars exceedingly amplified [34, 35]. A perturbation in the jet, a blob or a knot, might emerge near its base, which might cause these brightness variations.

Large-scale jets, on the other hand, are prominent, asymmetric, ending in plumes and two-sided, which is the case for FR I radio galaxies, or weak, often one-sided and end in radio lobes with bright hotspots that are seen on both sides, which is the case for FR II radio galaxies [20]. However, why exactly the jets are different in FR I and FR II galaxies is uncertain [36]. They can be either intrinsically different or environment affects them making them different from another [37, 38].

Variability connects with particle acceleration within the jet. There is the shock model, stochastic acceleration and magnetic reconnection that are able to explain jets and are relevant for studying jets [39–43]. The shock model can recreate the

observed power-law non-thermal particle spectrum that we see in blazar spectral energy distributions [44]. The part of the jet where the speed of the flow decreases from supersonic upstream speed to the subsonic downstream speed is usually defined as a shock [45, 46]. The second-order Fermi acceleration is the mechanism how the shock is thought to transport energy to particles. A particle will gain energy through crossing the shock front in this way: the particle will be scattered off of the irregularities within the plasma flow and will gain energy. To escape the shock a particle must cross upstream but with the velocities being close to the speed of light in the relativistic shocks the particle is caught up with the shock and actually forced to cross back downstream. If this crossing happens repeatedly, the energies can reach up to the TeV energy range.

In the real case of a blazar jet, however, the relativistic instance of the second-order Fermi acceleration has to be corrected further and it is thought to work through the particles crossing Alfvén waves frozen-in to the plasma. Due to this the shock model is not easily applied to the real case of the blazar jets. In addition, some of the simulations of this model lack the production of the high optical polarization observed in blazars, which we need to consider other mechanisms are also acting on the jet. [44, 46]

One of the other mechanisms acting on the jet is stochastic acceleration or first-order Fermi acceleration through turbulence [44, 47]. This mechanism is also capable of producing the observed power-law non-thermal particle spectra seen in blazars. The mechanism introduces a scattering agent needed to be present to force the particles to cross the shock front. The agent is usually thought to be plasma turbulence that causes resonant interactions of the particles through which the stochastic acceleration takes effect. During polarization-dependent radiation simulations the shock model is able to produce the polarization degrees above 40%–50% but not the ones at 10%–20% like the stochastic model can due to the turbulence [48]. However, the

stochastic model or a similar turbulent model requires shocks to cause the turbulence in the jet thus making it only a part of the solution for the acceleration in blazar jets [44, 47].

Lastly, there is a model of magnetic reconnection to explain the flaring activity in blazars [49]. This model theorizes that magnetic reconnection originates from kink instabilities to accelerate the jet particles. It has been accepted to be the main acceleration mechanism in the Sun but recently it has been studied more widely in AGN jets: it is capable of reproducing the high polarization degree and angle swings as well as the typical blazar SED [44]. The magnetic energy from the jet emission region is released and it heats the plasma and accelerates the particles when two field lines of opposite polarity get close to each other and annihilate because of the instabilities in the environment surrounding them [44, 50]. This is magnetic reconnection and it can be very effective method to get the particles accelerated. It is theorized to work through leptons, and models using it seem to explain the multi-timescale variability seen in blazars through the flares well [51, 52].

1.4 The optical-VHE band variability

Optical emission has been studied since the first discovery of BL Lac objects. It started with observing the variability of BL Lacertae that was without regularity, first classified as a variable star and later distinguished to be similar to quasars [53, 54]. Because the jet is Doppler boosted, the emission from the jet is the dominative component in blazar SEDs and the optical emission can be seen in the flat part of the synchrotron component [13]. In BL Lacs most of the observed optical emission has an origin in the synchrotron emission of the jet, however, the host galaxy contributes to this emission in HBLs due to low redshifts and in LBLs in their non-flaring states when the emission from the jet is weaker [55].

Blazars have very high variability in the optical band [55]. The variability time

scales are of hours to days to years. Multi-wavelength variability studies help constrain the size of the emission region, jet geometry and jet acceleration mechanisms [56]. A multi-wavelength light curve of very bright object Markarian 421 (Mrk 421) is shown in Figure 3 [57]. There is a light curve in multiple bands all the way from VHE to radio. In Mrk 421, X-rays and VHE gamma-rays have been found to correlate [56].

The variability between wavebands has previously only been able to be done with a limited sample of the brightest blazars. This has since been made easier by Fermi LAT gamma-ray satellite in gamma-ray band up to the high energies, and the current generation of Imaging Air Cherenkov Telescopes (IACTs) H.E.S.S., MAGIC and VERITAS have increased the number of VHE gamma-ray blazars. Thanks to these new instruments, the VHE gamma-ray observations are often triggered by flares observed in other wavebands. Due to this, other dedicated, poorer sensitivity monitoring telescopes such as Whipple and FACT are a crucial addition when studying the long term variability of blazars in VHE. [32]

There has been studies on connections between different wavebands, typically between optical and radio where they include correlation functions, especially Discrete Correlation Function (DCF), to study the characteristic time scales of sources by the use of autocorrelation and the correlations between two wavebands. In addition, an association of ultra-high-energy neutrinos to blazars has been made which has lead to hadronic emission models to be developed for the jet since neutrinos are the end products of proton-photon interaction. In other words, this process needs energetic protons to be present and these energetic protons would be accelerated to high energies in the jets. [32]

In this thesis I am investigating the connection of VHE and optical bands by trying to find correlation between VHE flux states and optical flares, which would hint a common origin for both VHE and optical emission. To find the correlation I

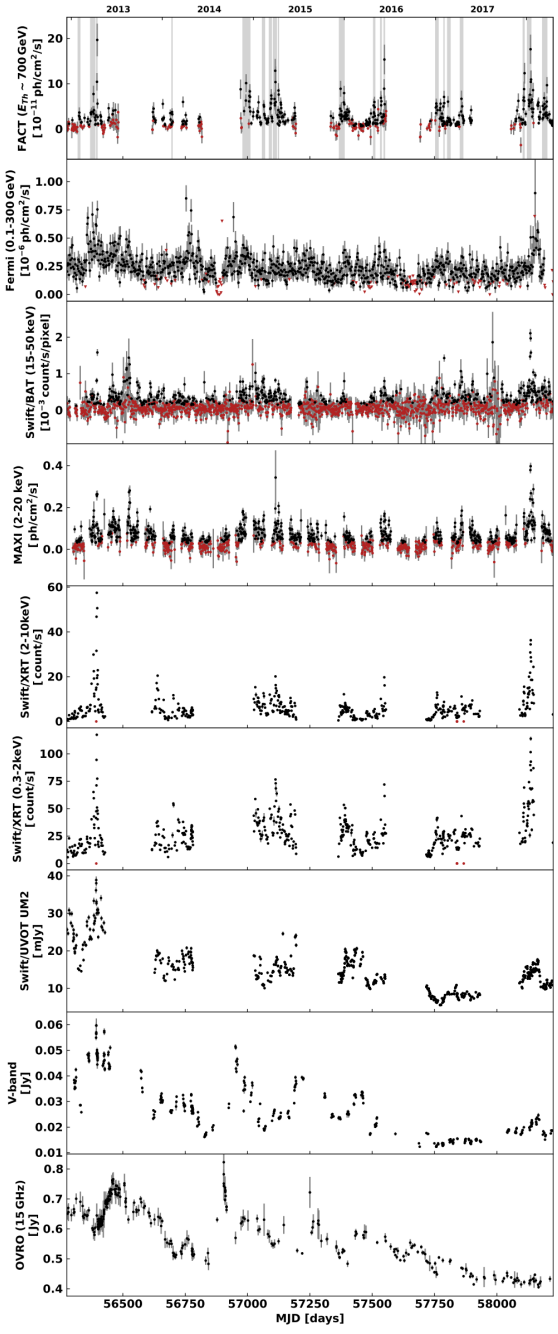

Figure 3: Long-term light curves of Mrk 421 obtained from the radio to the TeV range between December 14, 2012 and April 18, 2018. The first light curve is the FACT VHE light curve above 700 GeV energy threshold and the second is the Fermi LAT light curve from 0.1 GeV to 300 GeV. The third to the fifth light curve are X-ray light curves: the MAXI light curve (2–20 keV), the light curve of BAT of Swift (15–50 keV) and the light curve of XRT of Swift (0.3–2 keV), respectively. The sixth light curve is the ultraviolet light curve of UVOT of Swift using band UVM2. The seventh light curve is the optical V-band observations done with 1.54m Kuiper Telescope on Mountain Bigelow and the 2.3m Bok Telescope on Kitt Peak. The eight and last light curve is the radio observations at 15 GHz done with OVRO. Vertical grey bars represent flux measurement errors and points with signal-to-noise ratio lower than two are coloured red. For the FACT light curve there are 177 out of 580 such point and the flares determined by Arbet et al. (2021) are highlighted in grey. The triangles in the Fermi LAT light curve are 95% flux upper limits. [57]

can not use typical methods for cross-correlation like DCF because either the VHE gamma-ray light curve of a source is very poorly sampled or does not exist at all due to having been detected just once. So first, I try to characterize the optical variability timescales, and then try to see if I can find correlation between the VHE flux states and optical flares.

2 Optical data and analyses

In this part of the project, the goal was to determine optical flares of a sample of blazars and find out if there were any duration of an optical flare of a blazar that was prominent in the dataset. This was done because we wanted to use a common time period for each VHE flaring state in the VHE-optical comparison. To determine the flares from the optical light curves, I used Bayesian blocks method and hill-climbing algorithm. For this flare determination, I used a Python script originally written by Yannis Liodakis. After having determined all the flares, I used statistical visualization to see if there were such duration that was distinguishable from others.

2.1 Observational data

The optical data used in this thesis are mainly from the Tuorla Blazar Monitoring Program that began in 2002 [58]. However, due to lack of data from the program for some of the blazars, other sources of optical data were used. This data was only used for the second part of the project and is discussed in more detail in section 2.1.1. The Tuorla Blazar Monitoring program was launched as optical support program for the very high energy (VHE) gamma-ray observations by the Major Atmospheric Gamma Imaging Cherenkov (MAGIC) Telescopes.

The program used the Tuorla Observatory 1.03 m telescope located in Piikkiö, Finland from 2002 to 2004. In 2004-2020, the 35cm Celestron attached to the main telescope of the Kunliga Vetenskapsakademien (KVA) Observatory located at the island of La Palma, Spain was the main telescope of the program. From 2021 the program started to use the 80 cm Joan Oró Telescope (Telescopi Joan Oró, also known as TJO, in Spanish) at Montsec Astronomical Observatory in Spain. Observations have been performed during every clear night, but cadence for individual targets is irregular, typically aiming at least 1-2 observations per week. All of the observations are done in Cousins R-band. For the data analysis, the bias and dark

images are taken each night, and the flat-field images are taken every month, or in the case of TJO, every night. The data were analyzed using a semi-automatic pipeline for differential photometry [59]. In addition, there are scripts to subtract the host galaxy contribution from the results and correct them for galactic extinction [1].

The sample for the analysis of the optical data consists of 53 blazars that were observed in the optical Johnson-Cousins R-band between 2002-2021. Every blazar in the sample have also been detected in the VHE band in the TeV range. The sample of blazars is listed in Table 1. The sample was selected from the Tuorla Monitoring program based on optical data availability and optical variability. We needed to have sources which had optical data taken over a long period so all of the sources in our sample have at least 5 years of data as can be seen in Table 1. We also wanted data preferably with minimal breaks in between observations for the Bayesian block program to give the best results. The Table includes the name, the right ascension (RA) and the declination (DEC) of each blazar as well as the number of data points in their light curve, the duration of the light curve and number of seasons it was divided into. A sample light curve of blazar Markarian 421 is shown in Figure 4 where the time is in Julian days and the brightness is flux in janskys (Jy). It shows small error bars in terms of the flux and seasonal gaps throughout the observations as well as variability. In the middle of the light curve one can clearly see a very large flare as well as smaller ones on the sides.

On the other hand, Figure 5 shows the light curve of B3 2247+381, which has larger error bars and smaller amplitude changes than Figure 4, making it harder to separate flares. The seasonal gaps are present in the light curve.

[1]Host galaxy correction means that for some low-redshift blazars ($z< 0.3$) in our sample the host galaxy is bright enough to contribute significantly to measured flux and has to be corrected for, see Nilsson et al. 2007 [60]. Galactic extinction is the part of the radiation emitted by the blazar that is absorbed by the dust in our galaxy.

These seasonal gaps are seen in every light curve because in the optical observations there is a roughly 180–200 day season in which the source is not observable during the night. This was accounted for by dividing each source by season and handling every season separately for the final analysis. A season was set to be equal to or longer than 90 days. The gaps are a problem when attempting to estimate the duration of the flare because there might be a gap in the data before the end of the flare, or the flare might have started during the gap.

Table 1: The first part of the sample of blazars used for the optical data analysis. The Table includes the names of the blazars as they are in the Tuorla program, the right ascension (RA) of the sources, the declination (DEC) of the sources, number of data points in their light curve, duration of the light curve in years and the number of seasons they were divided into.

Blazar name	RA	DEC	Number of data points	Duration of the light curve [yr]	Number of seasons
1ES 0033+595	00 35 52.6	+59 50 05	625	18.67	19
1ES 0229+200	02 32 48.6	+20 17 17	327	13.37	14
1ES 0414+009	04 16 52.5	+01 05 24	249	11.24	14
1ES 0502+675	05 07 56.2	+67 37 24	350	11.11	13
1ES 0647+250	06 50 46.5	+25 03 00	522	18.38	20
1ES 0806+524	08 09 49.2	+52 18 58	540	17.27	18
1ES 1011+496	10 15 04.2	+49 26 01	675	17.10	18
1ES 1218+304	12 21 21.9	+30 10 37	445	16.94	18
1ES 1426+428	14 28 32.6	+42 40 21	374	16.94	18
1ES 1440+122	14 42 48.3	+12 00 40	97	5.49	6
1ES 1741+196	17 43 57.8	+19 35 09	422	14.88	15
1ES 1959+650	19 59 59.8	+65 08 55	1253	18.68	19
1ES 2037+521	20 39 23.5	+52 19 50	153	3.54	4

1ES 2344+514	23 47 04.8	+51 42 18	672	18.18	20
3C 66A	02 22 39.6	+43 02 08	927	17.16	19
3C 279	12 56 11.1	-05 47 22	684	18.52	18
AP Lib	15 17 41.8	-24 22 19	134	7.53	7
B2 0218+35	02 21 05.5	+35 56 14	188	6.65	9
B3 2247+381	22 50 05.7	+38 24 37	533	13.56	15
BL Lac	22 02 43.3	+42 16 40	1235	17.33	19
H 1722+119	17 25 04.3	+11 52 15	620	15.09	17
HB89 0317+185	03 19 51.8	+18 45 34	226	9.16	16
HB89 1749+096	17 51 32.8	+09 39 01	142	14.54	11
MG4 J200112+4352	20 01 12.9	+43 52 53	357	9.30	10
Mkn 180	11 36 26.4	+70 09 27	570	16.95	18
Mkn 421	11 04 27.3	+38 12 32	1124	18.43	19
Mkn 501	16 53 52.2	+39 45 37	1297	18.68	19
MS 1221.8+2452	12 24 24.2	+24 36 24	124	6.79	9
NVSS J073326+515355	07 33 26.8	+51 53 56	41	1.76	3
OJ 287	08 54 48.9	+20 06 31	1053	18.44	20
ON 231	12 21 31.7	+28 13 59	350	14.76	15
ON 238	12 24 54.4	+21 22 46	271	12.91	13
ON 246	12 30 14.1	+25 18 07	84	4.64	6
ON 325	12 17 52.1	+30 07 01	476	16.94	18
OT 546	17 28 18.6	+50 13 10	703	17.12	18
PG 1424+240	14 27 00.4	+23 48 00	441	14.91	16
PG 1553+113	15 55 43.0	+11 11 24	994	16.06	17
PKS 1441+25	14 43 56.9	+25 01 44	180	6.28	7
PKS 1510-089	15 12 50.5	-09 06 00	758	13.87	15
PKS 2155-304	21 58 52.0	-30 13 32	371	15.39	17
RGB 0136+391	01 36 32.7	+39 06 00	585	18.18	19

RGB 0214+517	02 14 17.9	+51 44 52	491	18.18	19
RGB 0710+591	07 10 30.1	+59 08 20	62	11.12	8
RGB 0847+115	08 47 12.9	+11 33 50	133	9.19	10
RGB 1136+676	11 36 30.1	+67 37 04	424	16.95	18
RGB 1719+177	17 19 13.0	+17 45 06	446	10.57	12
S2 0109+22	01 12 05.8	+22 44 39	126	5.30	6
S4 0954+65	09 58 47.2	+65 33 55	360	13.14	14
S5 0716+714	07 21 53.4	+71 20 36	843	17.66	19
TXS 0506+056	05 09 25.9	+05 41 35	77	3.50	5
TXS 1515-273	15 18 03.6	-27 31 31	37	0.49	1
VER 0521+211	05 21 45.9	+21 12 51	186	10.39	13
VER 0648+151	06 48 47.6	+15 16 25	162	9.15	11

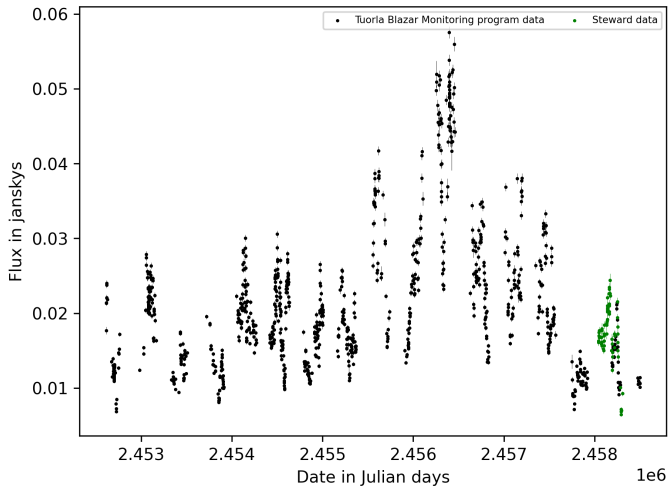

Figure 4: The light curve of the blazar Markarian 421. The data is from 06/12/2002 to 05/05/2021. This is an example of a well-sampled dataset with small error bars in terms of the flux, which is normal for a very bright target such as this one. The seasonal gaps in observations are clearly seen in the light curve.

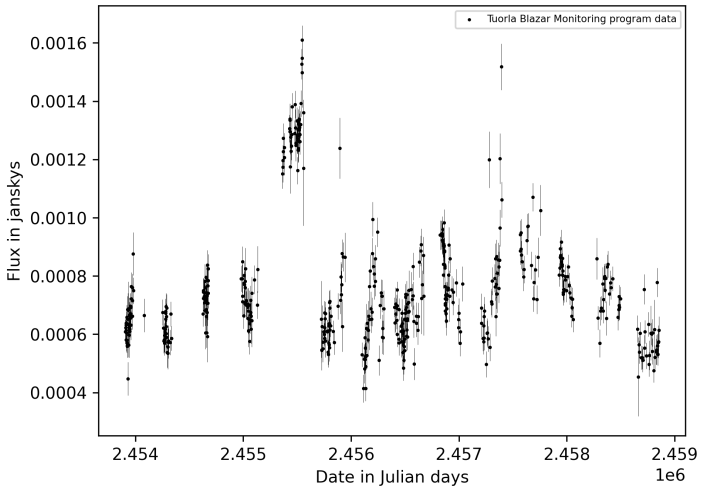

Figure 5: The light curve of the blazar B3 2247+381. The data is from 19/06/2006 to 01/04/2020. This target is a dimmer source compared to Markarian 421, and the data is quite spread out and has larger error bars compared to the light curve of Markarian 421. The seasonal gaps in observations are clearly seen in the light curve as were in the case of Markarian 421.

2.1.1 Combining light curves from multiple instruments

Combining light curves from multiple instruments was required for some of the sources due to the lack of data points but combining photometric data from different telescopes requires caution. It is extremely important to know what the different apertures used are, what kind of filters they use and if the filters are similar to each other. The magnitude system used affects the zeropoint of flux to magnitude conversion and the host galaxy correction depends on aperture and filter. This information is not always available, which is why I had to look for simultaneous nights between the different data sets to figure out if there were a significant difference in the fluxes.

Table 2 contains the blazars that had optical data taken from multiple sources: the Tuorla monitoring program (marked as KVA, even if it contains data also from Tuorla and TJO, see section 2.1.) [58], the Katzman Automatic Imaging Telescope (KAIT) [61], Zwicky Transient Facility (ZTF) catalog [62], Siena University Telescope (Siena) [63], Montarrenti Observatory (Montarrenti) [63], the Goddard Robotic telescope (GRT), Steward Observatory (Steward) [64], Catalina Real-Time

Transient Survey (CRTS) [65] and Michigan-Dartmouth-MIT Observatory (MDM) [66].

Table 4 contains information about the host galaxies and galactic extinctions of these sources. For blazar RX J0648.7+1516 (also known as VER 0648+151) I used four optical data points from Aliu et al. (2011) [67]. They used old galactic extinction value of 0.383 mag and I changed it to the new value of 0.313 mag. ZTF data of GB6 J1058+2817 was given in AB magnitudes and were converted to Vega magnitudes to be consistent with the rest of the data sample. The R band zero-magnitude flux density of 3080 Jy and the ZTF r-band zero-magnitude flax density of 3631 Jy were used for the magnitude to flux conversions. ZTF r-band is not the same as the R-band used by the other instruments, and the filter transformation is color-dependent. Because we did not know the color for GB6 J10158+2817 and we did not have simultaneous data between ZTF r-filter and KVA R-filter, the difference in colour was estimated to be -0.2 magnitudes, which is the generally accepted difference for typical colors of blazars. Therefore I subtracted 0.2 from the magnitudes before converting them to flux.

We also checked data between different telescopes taken on same nights to look for systematic shifts between the telescopes since it was not always clear that all data have been analyzed using the same aperture sizes, for example. This shift was subtracted from the magnitudes for the combined light curve. Between the data from Siena and Montarrenti, GB6 J1058+2817 had four data points on same nights and the flux was similar within error bars. The average shift was 0.027 magnitudes which I took into account. MG4 J200112+4352 had three data points on same nights with two of them having similar flux within error bars. The average shift was 0.093 magnitudes which I also took into account. The combined light curves were host galaxy and galactic extinction corrected.

For blazar S5 0716+714 we used the Tuorla data we had as well as optical data

from other instruments during one of the VHE observation windows for which we did not have Tuorla data for. Table 3 lists the all instruments we got optical data from for the source. Due to there being so many different instruments, it has its own Table. These instruments were 70-cm Maksutov Meniscus Telescope of Abastumani Astrophysical Observatory [68], a Planewave 60-cm CDK24 telescope of Burke-Gaffney Observatory of Saint Mary's University [69], the 70-cm Astronomical Reflecting Telescope 8 (AZT-8) with ST-7 and Ap7p detectors and once with ST-7 detector and polarization only of Crimean Astrophysical Observatory RAS (CrAO RAS) [70], the 76-cm Super Light Telescope (SLT) of Lulin Observatory in Taiwan [71], the telescope located in McDonald Observatory in Texas that is one of the identical set of 40-cm telescopes developed by Las Cumbres Observatory (LCO) [72], the 175-cm telescope of Perkins Observatory [73], the 200-cm Ritchey-Chretien telescope and the 50/70 cm Schmidt camera of Bulgarian National Astronomical Observatory also known as Rozhen Observatory [74], the 65-cm Zeiss achromatic refractor of The Central Astronomical Observatory of the Russian Academy of Sciences at Pulkovo, St. Petersburg [75], the 32-cm Maksutov-Cassegrain telescope of Siena University [63], the IAC80 telescope of Teide Observatory in Spain [76] and the 40-cm optical robotic telescope of Gravitational wave Optical Transient Observatory (GOTO) in Spain [77]. All of them were checked for simultaneous nights and multiple were found but Tuorla data did not have any simultaneous nights with the others. The R band zero-magnitude flux density of 3080 Jy was used to convert the magnitudes and the galactic extinction was taken into account while the host galaxy is very faint and thus it was not taken into account in the calculations. The shift in flux during simultaneous nights between the data from the different instruments, excluding Tuorla data, was less than 10^{-3} mag in each case. This leads us to conclude that the R band used in the observations is similar to the KVA R-band and the shift was discarded.

The data from other sources was given in either Vega or AB magnitudes. After converting the magnitudes to fluxes, they were host galaxy corrected if the host galaxy was deemed to be significant enough to affect the results and then converted back to magnitudes. After this the magnitudes were corrected for galactic extinction and finally converted to fluxes again and added in with the other data. The magnitude was converted to flux with the known formula

$$F_{\mathrm{R}} = F_0 \cdot 10^{-\frac{m}{2.5}}, \tag{1}$$

where F_0 is the zero-magnitude flux density in the given band, F_{R} is the flux in the given band and m is the magnitude in the given band. For the zero-magnitude flux density I used the R-band zero-magnitude flux density $F_{\mathrm{Vega},0} = 3080$ Jy for Vega magnitudes and $F_{\mathrm{AB},0} = 3631$ Jy for AB magnitudes. From the given magnitude m I got two different values by adding and subtracting the magnitude error m_{err}:

$$m_1 = m + m_{\mathrm{err}} \tag{2}$$

$$m_2 = m - m_{\mathrm{err}}. \tag{3}$$

Then I used equation 1 to get two flux values, F_1 and F_2, and to get an average value for the flux and the flux error I used equations

$$F_{\mathrm{R,avg}} = \frac{F_1 + F_2}{2} \tag{4}$$

and

Blazar name	Observatory/Catalog/Instrument								
	KVA	ZTF	KAIT	Montarrenti	Siena	GRT	Steward	CRTS	MDM
B2 1811+31	63	0	403	0	4	0	0	0	0
GB6 J1058+2817	0	137	0	13	6	0	0	0	0
MG4 J200112+4352	357	0	0	0	0	25	0	0	0
Mkn 421	1123	0	0	0	0	0	71	0	0
PKS 2155-304	370	0	0	0	0	0	126	0	0
RGB 0136+391	585	0	0	0	0	0	0	95	0
TXS 0506+056	77	0	231	0	0	0	0	0	0
VER 0521+211	186	112	0	0	0	0	0	0	0
VER 0648+151	161	0	0	0	0	0	0	0	4

Table 2: The amount of optical data points for each source that had data from multiple instruments in the light curve. The different data sources were the Tuorla Blazar Monitoring Program (marked as KVA, even if contains data also from Tuorla and TJO) [58], the Katzman Automatic Imaging Telescope (KAIT) [61] and Zwicky Transient Facility (ZTF) catalog [62]. Siena University Telescope (Siena) and Montarrenti Observatory (Montarrenti) [63], the Goddard Robotic telescope (GRT), Steward Observatory (Steward) [64], Catalina Real-Time Transient Survey (CRTS) [65] and the Michigan-Dartmouth-MIT Observatory (MDM) [66].

$$F_{\mathrm{R,err}} = \frac{abs(F_1 - F_2)}{2}, \tag{5}$$

where abs refers to the function to get the absolute value of the two flux values. Values $F_{\mathrm{R,avg}}$ and $F_{\mathrm{R,err}}$ were the values that were added with the other data to get the combined light curve.

Observatory/Catalog/Instrument	Number of data points
Tuorla	843
Abastumani	5
Burke-Gaffney	4
Crimean	15
Lulin	17
McDonald	1
Perkins	2
Rozhen1	1
Rozhen2	1
St. Petersburg	3
Siena	3
Teide	1
Tijarafe	15

Table 3: The amount of optical data points from each instrument for blazar S5 0716+714. KVA data is from the Tuorla monitoring program [58], Abastumani refers to the Georgian National Astrophysical Observatory or Abastumani Astrophysical Observatory [68], Burke-Gaffney data is from Burke-Gaffney Observatory of Saint Mary's University [69], Crimean refers to the data from the 70-cm Astronomical Reflecting Telescope 8 (AZT-8) of Crimean Astrophysical Observatory RAS (CrAO RAS) using three different cameras; 1) ST-7 detector and polarization only, 2) just Ap7p detector and 3) ST-7 detector [70], Lulin data is from the 76-cm Super Light Telescope (SLT) of Lulin Observatory in Taiwan [71], McDonald refers to the data from the telescope that is one of the identical set of 40-cm telescopes developed by Las Cumbres Observatory (LCO) located in McDonald Observatory in Texas [72], Perkins refers to Perkins Observatory data [73], Rozhen1 refers to the data from the 200-cm Ritchey-Chretien telescope of Bulgarian National Astronomical Observatory also known as Rozhen Observatory [74], Rozhen2 refers to the data from the 50/70 cm Schmidt camera of Rozhen Observatory [74], St. Petersburg data is from The Central Astronomical Observatory of the Russian Academy of Sciences at Pulkovo [75], Siena refers to Siena University data [63], Teide refers to the data from the IAC80 telescope of Teide Observatory in Spain [76] and Tijarafe refers to the data from the 40-cm optical robotic telescope of Gravitational wave Optical Transient Observatory (GOTO) in Spain [77].

Blazar name	Host galaxy correction [mJy]	Galactic extinction [mag]
B2 1811+31	0.15	0.108
GB6 J1058+2817		0.054
MG4 J200112+4352	0.095	1.219
Mkn 421	8.1	0.033
PKS 2155-304	1.17	0.047
RGB 0136+391		0.168
S5 0716+714		0.067
TXS 0506+056		0.235
VER 0521+211	0.247	1.481
VER 0648+151	0.252	0.313

Table 4: Host galaxy information and galactic extinctions in their respective bands. ZTF uses r-band that is not the same as the R-band that the others use so that had to be taken into account by subtracting the difference in colour between the two. For GB6 J1058+2817 it was estimated to be 0.2 mag and for VER 0521+211 it was calculated from simultaneous nights to be 0.00052 mag, which was deemed small enough to be discarded. Also, in one case ZTF data was in AB-magnitudes which was taken into account. KVA, Siena and Montarrenti data already was host galaxy corrected but for other data it had to be taken into account. GB6 J1058+2817, RGB 0136+391, S5 0716+714 and VER 0506+056 have very faint host galaxies thus they were neglected. MDM data of VER 0648+151 used 0.383 mag as galactic extinction which we updated to 0.313 mag.

2.2 Identification of flares in optical light curves

The Bayesian blocks method was first introduced by Jeffrey D. Scargle [78]. It is a time-domain algorithm for detecting localized structures or bursts, revealing pulse shapes and generally characterizing intensity variations. I used it for fitting the light curves to identify flares. In photon counting data, finding structures is quite problematic and this method acts as a potential solution. It suits our purpose because the method does not have a lower limit on which time scales of the detected variability are occurring [79]. The optical variability of blazars can vary from minutes to hours and from months to years, which makes this procedure excellent for blazar analysis. The Bayesian blocks method also tries to separate the observational errors from the statistically significant changes in the data. The method does not need any information on the smoothness or shape of the signal, and it tries to handle data that have gaps in between or are unevenly spaced. This helps the method to decompose the optical light curves that have seasonal gaps to flares.

To identify the flares, a Python script written by Yannis Liodakis [2] where the Bayesian blocks method is used along with a hill-climbing algorithm to find the individual flares in the light curves, is used. The light curves are divided based on the flux changes by the Bayesian blocks method. Then the hill-climbing algorithm determines the turning point per block where the flux density slope changes sign indicating a start, peak and end of the flare. The start time of a flare is defined as a point in time where the hill-climbing algorithm has recognized a change in the flux

[2]The script was written in Unix operating system in Python version 2 while I am using Windows 10 operating system with Python version 3. This introduced some weird issues and wrong results: some of the data arrays were cut out and the pathing was different. This forced me to make a few changes to the original script. I ran the script multiple times with different gamma values and with and without dividing the light curves by seasonal gaps. The first few runs were done with only six sources as they were the only ones available to use at the time but as soon as I received the rest of the data I included them in my script.

slope from negative to positive and vice versa for the peak of a flare. The end of a flare is then again defined by the point when the flux changes direction.

One of the strengths of the Bayesian Block method is that it has only one parameter that can be fine-tuned "by hand". It is the gamma parameter that can be anything from 0 to 1. Gamma is a geometric prior that assigns a smaller probability to a larger number of blocks [79]. It has an impact on the number of blocks in the optimal representation which makes it have an effect on the visual appearance of the representation and on values of quantities derived from it. In our case it can be seen as a simple way to modify the amount of structure in the block representation of the light curve. For a smaller values of gamma, a smaller number of blocks is a priori more likely than a larger number. The goal was to find out an optimal value for it which I did by running the script with different gamma values and plotting them to see how the parameter value affects the total number of fitted flares of all sources, similarly to what was done by Jenni Jormanainen in her master's thesis [80]. In addition, I compared how the gamma value affects the duration of the fitted flares.

Figures 6-7 present how the gamma value affects the number of flares. From Figure 6 one can see how much the number of flares grows when the gamma parameter increases. The slope is flatter, meaning that the number of flares fitted is closer to constant, with gamma values of 0.2–0.5 than with values < 0.2 or > 0.5. Jormanainen (2019) also arrived at a similar result [80].

We also investigated how the gamma factor affects the number of poorly defined flares. The start, peak and end times of a flare can not be securely defined if the flare consists of too few data points, which is why we remove all flares that consist of four data points or less. Figure 7 shows how many flares are removed due to having only four defining data points in the original light curve with different gamma values. It seems to be in agreement with the other slope but as it is produced with smaller

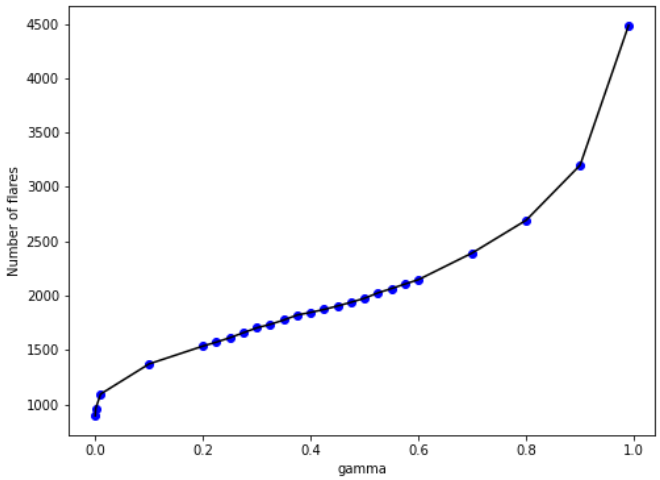

Figure 6: The number of flares as a function of the gamma parameter using all 53 light curves. Here the light curves are not divided into seasons.

gamma values, one can see that the amount of removed flares is more constant with gamma values of 0.1–0.2 but the flattening is really marginal. We focused our study for smaller gamma values of 0–0.4.

We want the least fitted flares, e.g. only the largest flares because these are the most defined flares overall as well as they are less likely to be falsely flagged as flares due to the algorithm. This means the lower gamma value the better but with very low gamma values (< 0.1) the number of fitted flares and the amount of removed flares changes rapidly with gamma. So the most optimal gamma value for the data set would then be around 0.1. Jormanainen (2019) found the most optimal value to be 0.2 which is also on the lower side but we wanted to lessen the amount of flares further as well as to get less shorter flares as they were usually defined by smaller amount of data points in general and these flares are more likely to not be real flares [80].

Figures 8-10 represent some examples of the light curves decomposed to flares. Figure 8 represents the fitted flares of the whole light curve of 1ES 0647+250 where the gamma parameter was 0.2 for the left side and 0.7 for the right side of the Figure.

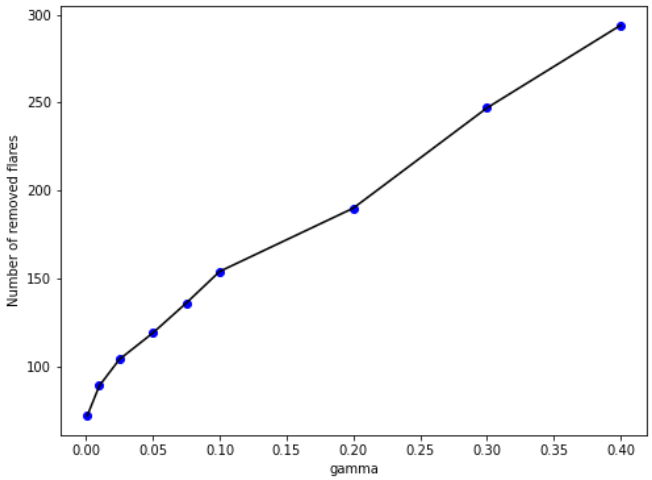

Figure 7: The number of removed flares as a function of the gamma parameter using all 53 light curves with dividing them into seasons. The removed flares are the flares that the hill-climbing does not detect anymore after removing flares that are defined by four or less data points.

There are 36 flares detected by the algorithm when the gamma value is higher and 24 when it is lower, which is a steep 50% decrease in flares. This seems to agree with our earlier analysis of the gamma parameter. These fits are done without dividing the light curve into observing seasons which also makes this many flares hard to see from the Figure.

Figures 9-10 show the results of the fitted flares for season 9 of 1ES 1959+650 and season 6 of 3C 66A, respectively. The gamma value used for pictures on the left was 0.1 and 0.4 for the pictures on the right. The different colored areas indicate different individual flares that the hill-climbing algorithm detected. Figure 9 demonstrates the difficulty of identifying very long flares that have duration longer than one observing season. In Figure 10, however, one observing season consists of many short flares. On the left side of the Figure the code found eleven flares while on the right side 12 flares were detected. The x-axis is the date in Julian days and the y-axis is the flux in mJy. This demonstrates the problem with the code on detection of flares very well: to the eye some of those flares do not seem like actual flares.

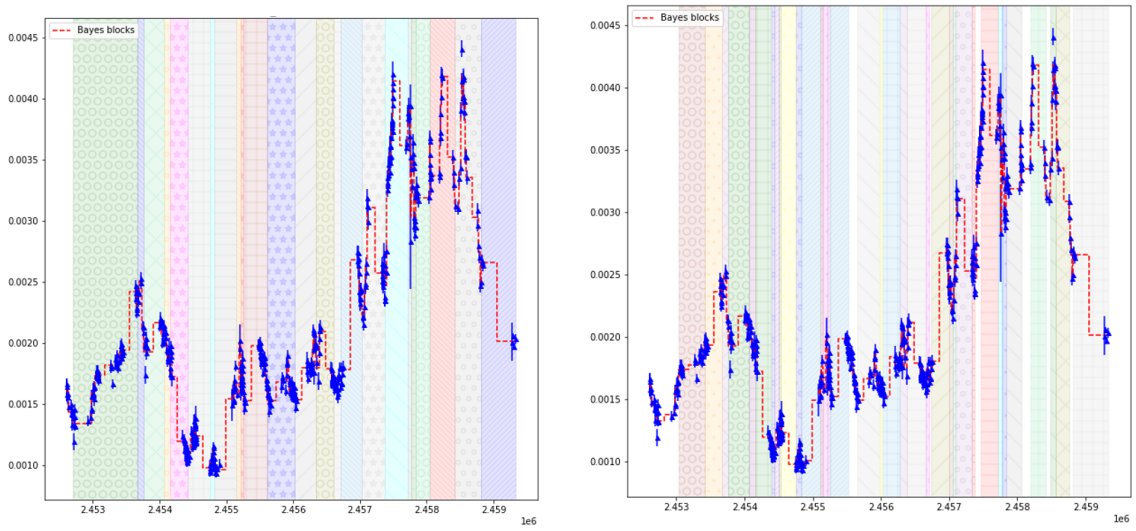

Figure 8: The fitted flares of the whole light curve of 1ES 0647+250 using gamma parameter values 0.2 (left) and 0.7 (right). The hill-climbing algorithm detected 24 flares on the left and 36 on the right. These are shown in the Figure as different colored areas. The error bars of the data is shown as blue and the red lines represent the Bayesian blocks. The x-axis is in Julian days and the y-axis is in flux in mJy. The light curve starts on December 7, 2002 and ends on April 19, 2021.

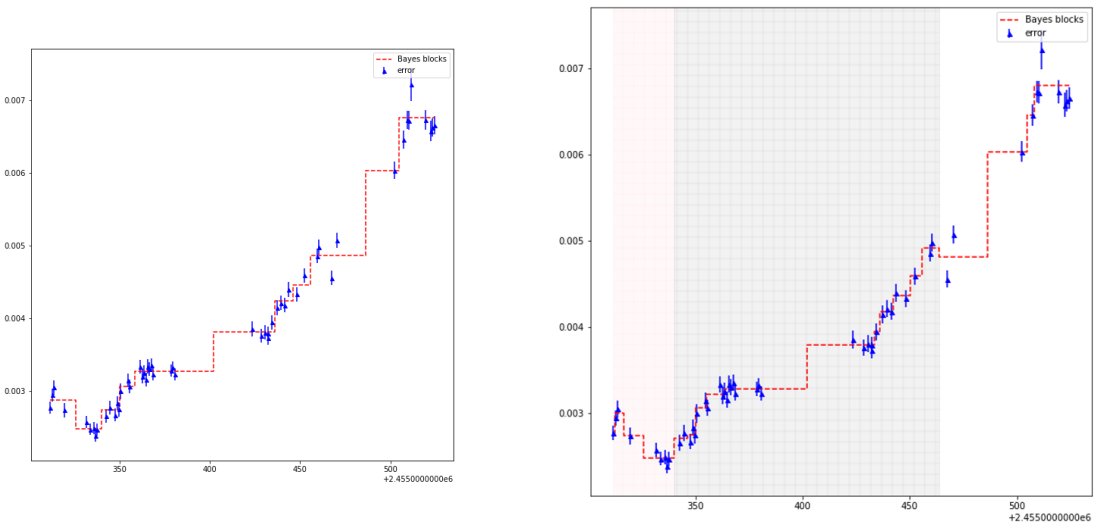

Figure 9: The fitted flares of the season 9 of the light curve of 1ES 1959+650 using gamma parameter values 0.1 (left) and 0.4 (right). The hill-climbing algorithm do not detect any flares on the left but in the right it detects one that is highlighted with the colored area. The error bars of the data is shown as blue and the red lines represent the Bayesian blocks. The x-axis is the date in Julian days and the y-axis is the flux in mJy. The light curve starts on April 25, 2010 and ends on November 16, 2010.

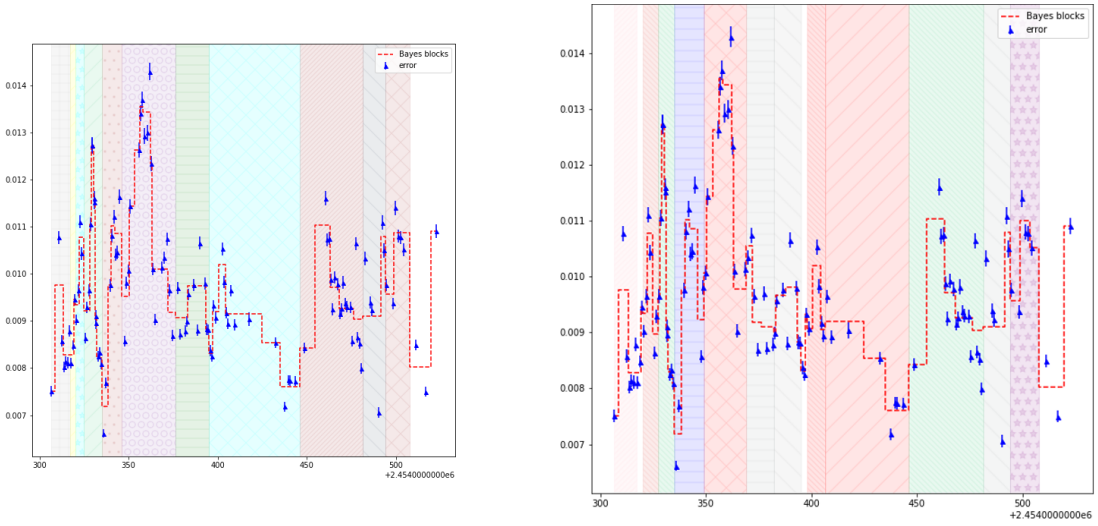

Figure 10: The fitted flares of the season 6 of the light curve of 3C 66A using gamma parameter values 0.1 (left) and 0.4 (right). The hill-climbing algorithm detected 11 flares on the left and 12 on the right. These are shown in the Figure as different colored areas. The error bars of the data is shown as blue and the red lines represent the Bayesian blocks. The x-axis is in Julian days and the y-axis is in flux in mJy. The light curve starts on July 26, 2007 and ends on February 24, 2008.

In summary, the code was run with several different gamma values and we found the optimal gamma value to be around 0.1. With this value we got rid of many short flares but not too many, which we wanted. We also got rid of flares that were not defined by many data points to avoid fake flares as well as divided the light curves into seasons to diminish flares that were very long and thus potentially wrongly detected by the algorithm.

2.3 Durations of flares

The duration of each flare in days was calculated by taking the start time from the end time in JD after decomposing the light curves to flares. These durations I then plotted to histograms for different gamma values. The histogram plots were produced using Python built-in method. I used multiple different gamma values and bin sizes. For the histograms, smaller bin sizes, e.g. how many series of intervals the range of durations were divided into, made it easier to see possible patterns in

the data. I also inspected how the amount of short flares depends on the gamma parameter. Here short flares mean flares with a duration of 25 days or less.

In Figure 11, I present the number of flares with different durations for four different gamma values: 0.0001, 0.01, 0.1, 0.2 and 0.4. The same Figure was also made using gamma values of 0.025, 0.05, 0.075 and 0.3. It is clearly seen that the higher the gamma parameter is, the higher the number of flares the hill-climbing algorithm detects, and vice versa.

However, with all different gamma values the shape of the histograms persists and the peak is in the bin, which consist of flares with duration of 15–20 days. Though, there is the significant caveat that as we described in previous section, we have removed all flares with less than 4 data points and these would mostly have duration of 0–10 days. Even given this significant caveat, we decided to use a window of two weeks for the optical data in the following part of this project because it is still the most common duration.

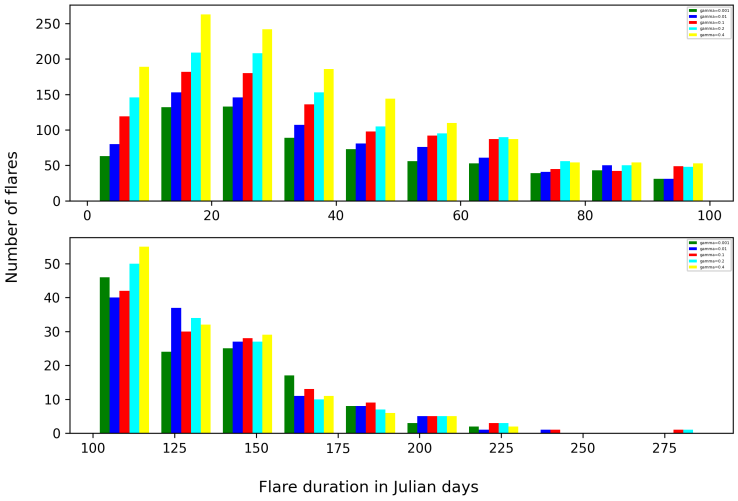

Figure 11: A histogram representing the different flare durations and number of flares with several gamma values. On the x-axis is the flare duration in Julian days and y-axis has the number of flares. The bin size used was 10.

3 VHE data and analyses

Very high energy gamma rays are observed with Imaging Air Cherenkov Telescopes (IACTs) that are capable of detecting gamma rays from tens of GeV up to the photon energies of ~ 50 TeV. The technique of the IACT is when a gamma-ray strikes the atmosphere, a cascade of relativistic charged particles is produced generating a very short flash of Cherenkov radiation and this is then imaged with large mirrors and high-speed cameras [81]. This cascade of charged particles is initiated at an altitude of 10–20 km. In the vicinity of the nucleus of an atmospheric molecule, the incoming gamma-ray photon undergoes pair production. The extremely high-energy electron-positron pair produced undergoes Bremsstrahlung immediately. This radiation produced is itself extremely energetic, with many of the photons undergoing further pair production. A cascade of charged particles ensues which, due to its extreme energy, produces a flash of Cherenkov radiation lasting a few nanoseconds.

In this thesis we have data from the Major Atmospheric Gamma Imaging Cherenkov (MAGIC) telescopes, the High Energy Stereoscopic system (H.E.S.S.), the Very Energetic Radiation Imaging Telescope Array System (VERITAS), the First G-APD Cherenkov Telescope (FACT), the Collaboration between Australia and Nippon for a Gamma Ray Observatory in the Outback (CANGAROO) I-III telescopes, the Whipple 10-meter telescope of the Fred Lawrence Whipple Observatory and the High-Energy-Gamma-Ray Astronomy (HEGRA) telescope.

In total there are 251 TeV sources from which ~ 70 are known blazars [82]. Some of these blazars have been observed only once while some have multiple observations. Actual light curves exist only for handful of sources. For this work, we have collected all VHE gamma-ray data from the literature and defined simple criteria to divide it to high and low states. These are then compared with optical flux state to see if optical and VHE high states and low states preferably happen at the same time.

3.1 Data collection

We collected VHE gamma-ray data for all TeV BL Lacs for this thesis work. The work was started with the references for VHE gamma-ray data given in Fallah Ramazani et al. (2017) [83] and with the excel file that was included in there. This file has since been updated with new detections. We also considered further references in online catalog TeVCat for each source [82]. For some targets I also got unpublished data by the MAGIC collaboration by private communication of V. Fallah Ramazani. There were a few cases where the data was taken from presentations held in conferences. In these cases the exact dates and fluxes had to be estimated from Figures. Some published papers were also missing exact dates and fluxes at times forcing me to estimate them based on the information given and from Figures shown in the papers. For few most prominent VHE blazars long term light curves were used directly.

The excel file consisted of 66 VHE BL Lacs from which we ended up with a sample of 35 blazars. The references for each source can be found in Tables 5-8. 31 sources were discarded due to the failure to meet two criteria: i) exclude sources with no VHE flux variability, meaning that the data which yielded in detection in the VHE band of the source has been collected within >3 months and it shows no significant flux variability, and ii) exclude sources with no optical variability, meaning that the modulation index of the source is 0.00. This was determined by Lindfors et al. (2016) [84]. Out of the 35 blazars six had some of their dates estimated from a plot or, for example, if it was told that a source was observed in February 2012 I estimated that to mean the whole month rather than just one day.

Within the sample of 35 VHE BL Lacs, 15 had only one VHE observation which we assumed to be a high state because nowadays in particular, the observations are usually triggered by high state in other bands such as the lower energy gamma-rays observed by Fermi-LAT satellite. For the others that had many observations, the

fluxes were not always given in same energy range. I converted the fluxes to be above the same energy threshold for comparison. This was done using the formula:

$$F_{\text{new}} = F_{\text{old}} \cdot (\frac{E_{\text{new}}}{E_{\text{old}}})^{1-\alpha}, \tag{6}$$

where F_{new} is the flux in the new energy threshold, F_{old} is the flux in the old energy threshold, E_{new} is the new energy threshold, E_{old} is the old energy threshold and α is the photon index of the source. For the error I used

$$s_{\text{F}_{\text{new}}} = \sqrt{(\frac{dF_{\text{new}}}{dF_{\text{old}}})^2 F_{\text{old,err}}^2 + (\frac{dF_{\text{new}}}{d\alpha})^2 \alpha_{\text{err}}^2}, \tag{7}$$

where $s_{\text{F}_{\text{new}}}$ is the error (standard deviation) of the new calculated flux, $F_{\text{old,err}}$ is the error of the old flux and α_{err} is the error of the photon index [85].

Sometimes the paper gave the flux in Crab units (C.U.) only. To convert these to cgs units, I used the Crab nebula flux measured by the MAGIC telescopes in Table A.5 in Aleksic et al. (2016) [86]. I used the values in Table A.5 columns 4 and 8, which include the integral sensitivity of the MAGIC telecopes obtained with the low zenith angle Crab Nebula data sample above a given energy threshold, column 4 in C.U. and column 8 in cgs units. For example if the flux was 10% C.U. above 150 GeV, in cgs units it would be roughly

$$\frac{28.6 \cdot 10^{-13} \text{ photons cm}^{-2} \text{ s}^{-1}}{0.0084} \cdot 0.1 \approx 3.4 \cdot 10^{-11} \text{ photons cm}^{-2} \text{ s}^{-1}. \tag{8}$$

Finally, for sources Mrk 421, Mrk 501 and PG1553+113 there exists a lot of VHE data from different telescopes with very different thresholds. For example MAGIC

observations typically have threshold around 150 GeV while for FACT it is around 700 GeV, so extrapolating would have resulted in very large error bars. Therefore, we decided that as there exists well sampled long-term light curves for these sources from single telescopes, we will simply use those for this work and exclude other data.

3.2 Determining the high and low VHE states

For the comparison between the VHE and optical fluxes we wanted to divide the VHE fluxes in low and high states. This was done to look at the optical flux during the VHE low and high states.

We had to come up with a rule on how we divide the VHE windows in high and low states. We wanted a simple way to divide the states into low and high states. To determine this division criteria we first checked if having the low state flux be 50% or less than the high state flux would work in our case. This turned out to be a good criteria since this made it so that the division difference would not be within the errorbars in the low and high state fluxes. An example of this division is seen in Figure 12 where you can clearly see where the high state flux is twice as much as low state flux.

We analysed the long term VHE light curves of the sources that show the most variability in the VHE band, Markarian 501 and 421, to see what kind of flux values there are and would this criteria work for them as well. For both of them I investigated how many VHE windows would there be if the high and low state fluxes would follow this criteria and came to the conclusion that the low state flux is 50% of the high state flux will work for them as well.

Tables 5–8 show the blazars that we conducted the VHE-optical comparison on. In the Tables there are the observation windows, integral VHE fluxes within said windows along with information on above which energy threshold were they derived and what the flux state is. All the references are also listed in the Tables. In the

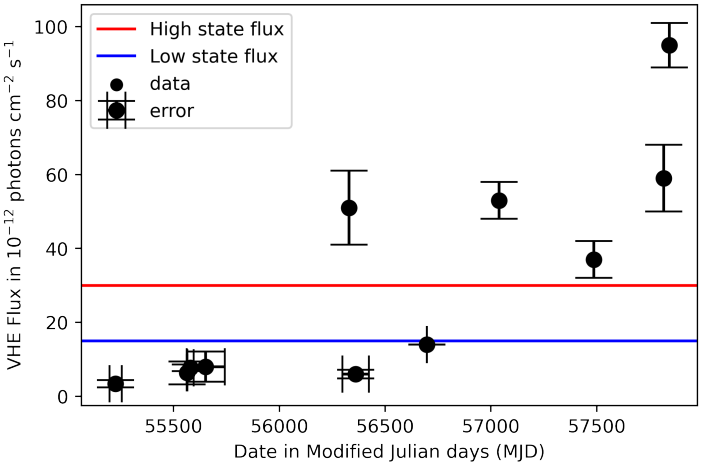

Figure 12: An example of how we divided the VHE flux states into high and low states. The red horizontal line shows the high state flux and the blue horizontal line shows the low state flux. The x-axis is in MJD and the y-axis is in 10^{-12} photons cm^{-2} s^{-1}. The VHE observation on MJD 56696 was excluded in the Figure for clarity of the picture due the VHE flux being so high ($(500 \pm 10) \cdot 10^{-12}$ photons cm^{-2} s^{-1}).

Tables there are four different numbered superscript notes to indicate the following. '1' indicates that the dates are either taken from a Figure and estimated, or the dates were not given exactly (e.g. only the year and the month was given) and are thus estimated. For example Jan 2010 would be a window from Jan 1, 2010 to Jan 31, 2010. This was done only if the observation window was a low state and not as significant to the VHE-optical comparison. '2' indicates that there is only one window of observations and within that window no significant flux variability was detected, and thus observation is marked as a high state. Also if this window was longer than 3 months, we discarded the source because VHE variability of the source was not certain. The selection of 3 months was data driven, it allowed us to keep most of the VHE gamma-ray data, but excluded VHE gamma-ray observations where observing windows would have been too wide. '3' indicates that there are several windows of observations but within those windows no significant flux variability has been detected, and thus all of the observations are marked as high states (has to be <3 months of observations). Finally, '4' indicates a merged window that will

be discussed in section 3.4.

The Tables also have one to four superscript asterisks related to flux values and they indicate the following: one asterisk (*) means that new flux in the new energy threshold was calculated from a previously given threshold using equation 6, and wherever necessary, unit conversion was also performed from Crab units (C.U.) to cgs units using Table A.5 in Aleksic et al. (2016) [86]. Two asterisks (**) means that the flux was converted from Crab units (C.U.) to cgs units, and three asterisks (***) means that the flux was taken from a Figure in the reference. Four asterisks (****) means that the fluxes in question will be reported in MAGIC Collaboration papers that are not yet published.

We discarded some of the sources on the original list seen on section 2 as well as some of the VHE observations based on five different exclusion criteria that we found necessary for the VHE-optical data comparison, two of which were already mentioned above. The criteria are: i) Exclude sources with no VHE flux variability, meaning that the data which yielded in detection in the VHE band of the source has been collected within >3 months and it shows no significant flux variability. ii) Exclude sources with no optical variability, meaning that the modulation index of the source is 0.00. iii) Exclude observations with a non detection ($> 5\sigma$ statistical significance). iv) If there are several high state flux points separated by less than two weeks, we handle them as single high state because this is the minimum window size that we use for calculating the optical average flux. We do this even if the source would have been at low flux state (within the error bars) in between. For example, in Figure 12 we see the flux states of ON325, and there the low state window MJD 56298–56424 is excluded because it overlaps with the high state window MJD 56330. If the time window of the observations is longer than 6 months or not clearly defined, we use the data only for VHE-VHE flux comparison (i.e. to check if there are periods where the VHE flux is >2*low state flux and qualify as high states). We do not use

these low states in the VHE-optical comparison. v) Finally, we also do not include the periods when the VHE flux is intermediate between the 'low' and 'high' flux to this comparison.

The first three criteria were quite obvious since we were looking for variable sources in both the VHE and in the optical bands where the VHE observational data actually yielded in statistically significant detection. We deemed more than six months of data without showing significant variability enough to state that the source was not variable during the observations. The fourth criteria was used similarly to the merged windows and to make sure that the uncertainty of the dates would not have an impact on the results. There were 84 high VHE flux states and 57 low VHE flux states in the final sample. All 35 sources had high states and 13 sources had low states.

Table 5: Most of the sample of blazars used for the VHE-optical comparison. There are three sources that have quite high number of observation epochs so they are represented in their own Tables. The Table contains the different VHE observations done for each source and the corresponding VHE fluxes given a certain threshold and the VHE flux states as well as the references to the original papers they are taken from. The dates are in modified Julian days (MJD) and the flux is in cgs units (10^{-12} photons cm^{-2} s^{-1}). The flux state of the source in each observation window is either low or high.

Blazar	Observation period [MJD]	Threshold [GeV]	Flux [10^{-12} photons cm^{-2} s^{-1}]	Flux state	References
1ES 0033+595	55060–55118	150	7.1 ± 1.3	high[2]	[87]
1ES 0647+250	54040–54190	300	$\lesssim 8.33$**	low[1]	[88]
	58820–58821	100	52.5**	high	[89]
1ES 0806+524	55616–55622	250	18.8 ± 3.9	high	[90]
1ES 1011+496	55616–55660	150	14.6 ± 1.6	low	[91]
	55958–56066	150	14.6 ± 1.6	low	[91]
	56691–56699	200	51–152**	high[4]	[92]
	56691–56723	200	230 ± 10	high[4]	[92, 93]
1ES 1218+304	54113–54178	200	12.2 ± 2.6	low[1]	[94]
	54829–54866	200	18.4 ± 0.9	low	[95]

	54861	200	57 ± 7	high	[95]
	54862–54944	200	18.4 ± 0.9	low[iv]	[95]
	58490	200	$(47.5 \pm 6.8)^*$	high	[96]
1ES 1959+650	54417–55862	300	$(35.9 \pm 6.9)^*$	low	[97]
	54382–54630	300	$(47.7 \pm 10.4)^*$	low	[97]
	55477–55688	300	$(47.7 \pm 10.4)^*$	low	[97]
	57571–57721	300	50^{***}	low[iv]	[98]
	57552–57553	300	400 ± 13	high	[98]
	57570–57581	300	376 ± 8	high	[98, 99]
	57507	300	272^*	high	[100]
	58000	300	50^{***}	low[1]	[101]
1ES 2344+514	53585–53597	300	$(14.7 \pm 2.5)^*$	low	[102]
	53610–53642	300	$(9.09 \pm 2.55)^*$	low	[102]
	53700–53736	300	$(10.7 \pm 2.5)^*$	low	[102]
	54377–54476	300	10.6 ± 0.9	low[4]	[103]
	54441	300	67.7 ± 0.6	high	[103]
	54442–54476	300	10.6 ± 0.9	low[iv]	[103]
	54759–54800	300	$(1.70 \pm 0.83)^*$	low	[104]
	54832–57387	300	$(9.34 \pm 0.54)^*$	low[1,i]	[105]
	57611	300	69 ± 9	high[iv]	[106]
	57612	300	22 ± 5	high[iv]	[106]
	57603–57615	300	29.3^*	high	[107]
3C 66A	54361–54746	400	1.73^{**}	low	[108]
	54747–54749	500	3.49^{**}	high	[108]
	54750–56604	400	1.73^{**}	low	[108]
	55170–55214	100	43.6^{**}	low	[109]
B2 1811+31	59126–59132	100	26.3^{**}	high	[110]
B3 2247+381	55469–55499	200	5.0 ± 1.7	high[2]	[111]
BL Lac	53583–53708	200	6 ± 2	high	[112]
	53936–54002	200	6 ± 2	high	[112]
	55740	200	$(3.4 \pm 0.6) \cdot 10^6$	high	[113]
	57188–57201	200	15 ± 2	high	[114]
	57666	200	$(4.2 \pm 0.6) \cdot 10^6$	high	[115]
	58606–58606	200	$\lesssim 20.3^{**}$	high	[116]
	59428	100	683^{**}	high	[117]
GB6 J1058+2817	59305	100	52.5^{**}	high	[118]
H 1722+119	56429–56434	150	$(6.81 \pm 1.70)^{**}$	high[2]	[119]
MG4 J200112+4352	55142–55161	200	5^{***}	low[iii]	[120]
	55383–55392	200	5^{***}	low[iii]	[120]
	55393	200	20^{***}	high[2]	[120]

	55394–55447	200	5***	low[iii]	[120]
Mkn 180	53817–53825	200	23 ± 7	high[2]	[121]
MS 1221.8+2452	56412–56413	200	8.12**	high[2]	[122]
OJ 287	57731–57777	150	< 7.63	high[iii]	[123]
	57785–57817	150	6.51 ± 0.93	high	[123]
	57827–57843	150	2.58 ± 0.91	low[iii]	[123]
ON 231	54466–54527	200	1***	low[iii]	[124]
	54528–54540	200	19.9 ± 0.7	high	[124]
	54541–54562	200	2***	low[iii]	[124]
	54624–54625	200	57 ± 6	high	[125]
	55200–56800	200	5***	high[i]	[126]
ON 246	57158–57163	100	(31.5–42.0)**	high[2]	[127]
ON 325	55197–55255	200	3.4 ± 1.0	low[1,iii]	[128]
	55565–55595	200	7.7 ± 0.9	low[1,iv]	[128]
	55563–55566	200	(6.35 ± 3.10)**	low[iv]	[129]
	55562–55742	200	8.0 ± 4.1	low[1]	[97]
	56298–56424	200	6.0 ± 1.2	low	[130]
	56330	200	51 ± 10	high	[130]
	56696	200	500 ± 10	high	[130]
	56697	200	< 14	low[iii]	[130]
	57039	200	53 ± 5	high	[131]
	57487	200	37 ± 5	high	[131]
	57817	200	59 ± 9	high	[131]
	57844	200	95 ± 6	high	[131]
OT 546	55687–55722	150	(5.79 ± 2.04)**	low	[132]
	56413–56419	300	18 ± 3	high	[106]
	57307–57327	250	11 ± 2	high	[133]
PKS 2155-304	53944–53949	200	(219 ± 109)*	high	[134]
	53200–53667	200	(50 ± 5)***	low[iv]	[135, 136]
	53704–53919	200	(50 ± 5)***	low[iv]	[135, 136]
	53969	200	141 ± 8	high	[135, 136]
	53952–53968	200	(50 ± 5)***	low[iv]	[135, 136]
	53970–54268	200	(50 ± 5)***	low[iv]	[135, 136]
	54269–54270	200	125 ± 14	high	[135, 136]
	54646–54650	200	115 ± 5	high	[135, 136]
	54651–54703	200	(50 ± 5)***	low[iv]	[135, 136]
	54705–55034	200	(50 ± 5)***	low[iv]	[135, 136]
	55035–55039	200	94.9 ± 6.9	high	[135, 136]
	55040–55529	200	(50 ± 5)***	low[iv]	[135, 136]
	55533	200	108 ± 20	high	[135, 136]

	55534–56246	200	$(50 \pm 5)^{***}$	low[iv]	[135, 136]
	56403–56601	200	$(5.15 \pm 1.47)^{*}$	low[iv]	[137]
	56805–56817	200	$(5.15 \pm 1.47)^{*}$	low	[137]
	57150–57330	200	50^{***}	low[1]	[138]
	57520–57620	200	30^{***}	low[1]	[138]
RGB 0136+391	55145–55156	150	2.71 ± 1.79	high[2]	[139]
RGB 0847+115	56629–56665	200	5.08^{**}	high[2]	[140]
RGB 1136+676	56686–56750	200	3.05^{**}	high[2]	[141]
S2 0109+22	57225–57231	100	47 ± 12	high[2]	[142]
S4 0954+65	57067–57082	150	20^{***}	high[2]	[143]
S5 0716+714	54406–54420	400	0.8 ± 0.7	high[3,iii]	[144]
	54578–54581	400	7.5 ± 2.2	high[3]	[144]
	57040–57050	150	$(89 \pm 11)^{***}$	high[3]	[145]
	57065–57070	150	60^{***}	high[3]	[145]
	58115	150	511	high[3]	[146]
TXS 0506+056	58020–58028	90	15.6^{**}	low[iv]	[147]
	58029–58030	90	67^{**}	high	[147]
	58031–58056	90	11.7^{**}	low[iv]	[147]
	58057	90	61 ± 12	high	[147]
	58058–58059	90	$\lesssim 4.95$	low[iv]	[147]
	58060–58155	110	20^{***}	low[i]	[148]
	58455	90	66.2–99.3^{**}	high	[149]
TXS 1515-273	58541–58547	400	$5.18 \pm 0.86^{**}$	high[2]	[150]
VER 0521+211	56242–56337	200	24 ± 2	low	[151]
	56580	200	$(70 \pm 7)^{***}$	high	[151]
	56625–56628	200	$(60 \pm 7)^{***}$	high[4]	[151]
	58904–58904	200	55^{*}	high	[152]
VER 0648+151	55259–55301	200	6.7^{**}	high[2]	[153]

Table 6: VHE observations taken by MAGIC for blazar PG 1553+113 for the VHE-optical comparison. The data has been compiled by Elisa Prandini (priv. comm). The dates are in modified Julian days and the flux is in cgs units (10^{-12} photons cm^{-2} s^{-1}). The flux state of the source in each observation window is either low or high.

Observation	Observation period [MJD]	Threshold [GeV]	Flux [10^{-12} photons cm^{-2} s^{-1}]	Flux state	References
1	53492–53507	150	$(71.4 \pm 20.4)^*$	high	[154]
2	53609–53614	150	150^*	high[iii]	[154]
3	53849–53860	150	$(60.9 \pm 18.7)^*$	high	[154]
4	53938–53943	150	$(64.6 \pm 16.9)^*$	high	[154]
5	59310	150	85^*	high	[155]
6	56043–56044	150	$(225 \pm 72)^*$	high	[156]
7	55268–55283	150	17.1	low	[157]
8	55354–55364	150	21.1	low	[157]
9	55983–55986	150	25.4	low	[157]
10	56018–56043	150	58.5	high	[157]
11	56420–56423	150	22.1	low	[157]
12	57180–57195	150	25.1	low	[157]
13	57238–57240	150	17.0	low	[157]
14	57422–57430	150	21.9	low	[157]
15	57450–57466	150	23.1	low	[157]
16	57541–57565	150	58.1	high	[157]
17	57570–57598	150	25.7	low	[157]
18	57603–57608	150	22.5	low	[157]
19	57790–57812	150	23.9	low	[157]
20	57816–57843	150	24.6	low	[157]
21	57846–57868	150	27.7	low	[157]
22	57875–57904	150	28.2	low	[157]
23	57947–57959	150	25.3	low	[157]

Table 7: VHE observations for blazar Mkn 421 for the VHE-optical comparison. The flux state of the source in each observation window is either low or high: intermediate states were discarded. The observations are the same ones reported by Arbet-Engels et al. (2021) [57] which are taken from [158]. The dates are in modified Julian days and the flux is in cgs units (10^{-12} photons cm^{-2} s^{-1}). The average flux of these was calculated to be $(19.86 \pm 6.87) \cdot 10^{-12}$ cm^{-2} s^{-1} which was defined as the low state. Thus the high state is $\gtrsim 40 \cdot 10^{-12}$ cm^{-2} s^{-1}.

Observation	Observation period [MJD]	Threshold [GeV]	Flux [10^{-12} photons cm^{-2} s^{-1}]	Flux state
1	56276–56317	700	20 ± 5	low
2	56371–56398	700	200 ± 30	high
3	56699–56976	700	30 ± 5	low
4	56986–57010	700	110 ± 10	high
5	57011–57054	700	40 ± 3	low
6	57065–57069	700	60 ± 15	high
7	57091–57125	700	120 ± 15	high
8	57368–57388	700	90 ± 10	high
9	57505–57511	700	80 ± 10	high
10	57533–57550	700	80 ± 10	high
11	57755–57762	700	70 ± 10	high
12	57770–57786	700	40 ± 5	low
13	57787–57789	700	80 ± 10	high
14	57814–57850	700	20 ± 3	low
15	57857–57865	700	90 ± 10	high
16	57866–58103	700	20 ± 3	low[iv]
17	58105–58137	700	150 ± 15	high

Table 8: VHE observations for blazar Mkn 501 for the VHE-optical comparison. The Table contains the different VHE observations done for the source and the corresponding VHE flux states. The dates are in modified Julian days and the flux is in Crab units (C.U.). The flux state of the source in each observation window is either low or high. All of the observations are taken directly from a long term light curve put together by Lea Hackmann (priv. comm). The spectrum for this source is similar to that of the Crab Nebula and therefore we use the fluxes in Crab units directly.

Observation	Date	Flux [C.U.]	VHE flux state
1	53519–53549	0.40 ± 0.07	low
2	53552–53564	1.40 ± 0.11	high
3	53566–53567	0.38 ± 0.04	low
4	54554–54599	0.25 ± 0.06	low
5	54913–54948	0.40 ± 0.10	low
6	54952	1.58 ± 0.10	high
7	54975–55038	0.36 ± 0.05	low
8	56007–56076	0.80 ± 0.04	low
9	56087	3.23 ± 0.07	high
10	56391–56479	0.30 ± 0.03	low
11	56483	2.69 ± 0.13	high
12	56831	6.51 ± 0.0	high
13	56854–56870	1.20 ± 0.0	low
14	53935–54005	0.35 ± 0.0	low

3.3 Source notes

Below are some details on sources and data that we discarded from this study. These follow the criteria defined in the previous section. I also make notes about

the amount of data for these sources.

1ES 0033+595: There is only one observation at VHE gamma-ray band for this source reported in literature. The epoch is $\sim$ 58 days and within that no significant flux variability has been detected; thus observation is marked as a high state.

1ES 0229+200: This source was found to be non-variable [84] in the optical band and therefore excluded from the study by the second criteria.

1ES 0414+009: The source was observed at VHE gamma-ray band by H.E.S.S. from MJD 53646 to 55159 [159] and by VERITAS from MJD 54466 to 55563 [160] and during both observations no significant flux variability was found. Since the source was observed over three months in the VHE band and no significant flux variability was found, the source is excluded by the first criteria.

1ES 0502+675: We could find only one observation in literature: a long observation period of $\sim$ 130 days (MJD 55097–55227) with no significant flux variability. Therefore, it does not meet the criteria of single short observation (<3 months) or significant variability [161, 162] and is excluded.

1ES 0647+250: The source has 6 observations at VHE gamma-ray band reported in literature but due to our criteria two non detections [88] and two observations during intermediate flux states [163] are excluded as well as HEGRA observations for which we did not have optical data for [164]. We have one observation that fit our criteria, in which the source is in higher flux state since the non detections clearly show lower flux state. Note that the non detections and intermediate states are not used in the VHE-optical comparison, only for VHE-VHE flux state comparison.

1ES 0806+524: There are 5 observations at VHE gamma-ray band for this source reported in literature. Two of them are excluded by the first criteria [162, 165] and two of them are intermediate flux states [165, 166]. The only observation that meets our criteria is clearly a high state compared to the earlier observations of the source (see Table 5).

1ES 1011+496: There are 6 observations at VHE gamma-ray band for this source reported in literature. Two of them are intermediate states [93, 167] and are discarded. One observation by VERITAS [92] and one by MAGIC [93] are emerged as one high state for the VHE-optical comparison. The other three observations are seen in Table 5.

1ES 1218+304: There are 10 observations reported at the VHE gamma-ray band in literature from which three are intermediate states [96, 168], two observations lack data about the flux thus could not be used [169] and one is a non detection by TACTIC [170]. The rest can be seen in Table 5.

H 1426+428: The source, also known as 1ES 1426+428, was observed over a long period of time in which its flux seemed to have varied. However, we do not have optical data during the whole of the period and for the period we do have optical data for, the source flux did not vary significantly. Therefore the source is discarded by the first criteria.

1ES 1440+122: The dates for the observations of this source were not publicly available. The source is excluded by the first criteria due to the VHE observation campaign lasting longer than six months and it was reported to not have any significant flux variability in that time.

1ES 1741+196: The source was observed over multiple years in four different observation windows and no significant variability was found. Therefore it is discarded by the first criteria.

1ES 1959+650: There are 12 observation windows at VHE gamma-ray band found in literature and during four of them the flux is in intermediate state [101, 171]. Observations done by Aharonian et al. (2003) as well as Krawczynski et al. (2004) are low or intermediate states but we have no optical data within them so they are excluded from the VHE-optical comparison [172, 173]. During observations MJD 557507–57539 from Acciari et al. (2020) the source is said to be on low state but

it is excluded because Buson et al. (2016) reported the source to be on high state on the overlapping MJD 57507, which is kept for the VHE-optical comparison [100]. Flares on MJD 57552 and 57553 as well as MJD 57570 and 57581–57581 are marked as single high states by the fourth criteria. The rest of the observations are seen in Table 5.

1ES 2037+521: This source was found to be non-variable [84] in the optical band and therefore excluded from the study by the second criteria.

1ES 2344+514: In literature, there are 11 observations reported at the VHE gamma-ray band from which two are merged (MJD 57611 and 57612) and included in the high state on MJD 57603–57615 for the VHE-optical comparison. All of the observations are seen in Table 5. Whipple and HEGRA VHE observations [174, 175] are not included because there were no optical data available during the VHE observations.

3C 66A: There are four observations at the VHE gamma-ray band, and the observation on MJD 54750–56604 by Furniss et al. (2015) is excluded by the first criteria [108]. All of the observations are seen in Table 5.

AP Lib: Only one detection in the VHE band reported in literature and no significant flux variability was detected, thus it is marked as a high state. We lack optical data during the observation and none is found in literature, so this source is discarded.

B2 1811+31: We did not have optical data for this source from the Tuorla blazar monitoring program, but wanted to include it for the VHE-optical comparison. The source is known as J1813+3144 in KAIT, where the optical data was taken from [176]. The source has one observation at the VHE gamma-ray band reported in literature and thus it is marked as a high state.

B3 2247+381: There is only one detection in the VHE band reported in literature, the observation window was $<$3 months and no significant flux variability was

detected during that time window: the single observation is marked as a high state.

BL Lac or BL Lacertae: There are 9 clear observations in the VHE gamma-ray band reported in literature and all of them are done during a high state flux of the source. We have to exclude the observations on MJD 59072–59081 reported by Blanch (2020) and the observations on JD 59111 reported by Blanch (2020b) because we do not have optical data within those windows even within ±7 days from the middle point of the windows since their duration is less than 14 days [177]. The rest of the observations are seen in Table 5.

GB6 J1058+2817: The source was detected by the MAGIC telescopes very recently and no previous VHE observations existed. The single observation is marked as a high state.

H 1722+119: There is only one detection in the VHE band reported in literature and no significant flux variability was detected during that time window: the single observation is marked as a high state.

HB89 0317+185: The source, also known as RBS 0413, was observed in VHE gamma-ray band over two campaigns: one lasting for almost three years while the other one lasted for almost a year, both of them resulting in flux variability that was insignificant. Thus, it is discarded by the first criteria.

MG4 J200112+4352: There are four observations in the VHE gamma-ray band reported in literature and three of them resulted in a non significant detection: the single observation is marked as a high state [120].

Mkn 180: There are two observational campaigns in the VHE gamma-ray band for this source: MAGIC ICRC 2011 proceedings were published but the Mkn 180 fluxes were not so they are excluded and the other observation is included. No significant flux variability was detected during the observation; thus, the single observation is marked as a high state [121].

MS 1221.8+2452: There is only one observation at the VHE gamma-ray band

reported in literature and no significant flux variability was detected during that time window: the single observation is marked as a high state.

NVSS J073326+515355: The source, also known as PGC 2402248, is also excluded by the first criteria. It has only one observation window lasting a little over three months which also shows no significant VHE flux variability.

OJ 287: There are three observations at the VHE gamma-ray band reported in literature. ATel#10051 reported significant VERITAS detection between MJD 57785–57788 which was around 1% C.U. above 150 GeV [178] and O'Brien (2017) reported significant detection between MJD 57785–57817 which was around 1.8% Crab above 150 GeV [123]. Since ATel is the preliminary analysis about the observation in general, I decided to only include the paper with the full analysis and observations reported. Only one observation with significant detection was found (MJD 57785–57817) but no significant flux variability was detected during the window; thus, the single observation is marked as a high state. All three observations are seen in Table 5.

ON 231: There are two observations at the VHE gamma-ray band reported in literature. Both of the windows were found with similar flux so both of them are marked as high states. The observations are seen in Table 5.

ON 246: There are only one observation at the VHE gamma-ray band reported in the literature. This consists of detections on three separate nights with no flux variability: the single observation is marked as a high state.

ON 325: In literature, there are 13 observations at the VHE gamma-ray band reported, of which one by Abeysekara et al. (2017) is done during an intermediate flux state of the source [130]. Observations by Aleksic et al. (2013), Mariotti (2011) and Aliu et al. (2013) are merged as one due to the fourth criteria [97, 128, 129].

OT 546: There are three observations at the VHE gamma-ray band reported in literature from which the earliest observation by Mariotti (2011) is clearly in a lower

flux state [132]. The observations can be seen in Table 5.

PG 1424+240: This is a very soft spectrum source with large error bars on the spectral index. Converting the fluxes from one energy threshold to another, none of the observations fulfill the criteria of the high state even if there seems to be variability in the VHE gamma-ray fluxes; thus, we have to exclude this source.

PKS 2155-304: There are 20 observations at the VHE gamma-ray band reported in literature from which two are done during an intermediate state of the source and are excluded. Low state is $< 5 * 10^{-11}$ cm^{-2} s^{-1} and high state is $> 10 * 10^{-10}$ cm^{-2} s^{-1} above 200 GeV. Because of the fourth criteria only the high state observation by FACT on MJD 53944–53949 is used for the VHE-optical comparison, and thus MAGIC and HESS observations represented by Aleksic et al. (2012) [179] and Aharonian et al. (2009) [180] as well as Aharonian et al. (2007) [181], respectively, are excluded. We did not find any optical data for VHE windows on MJD 53668, 54293–54624 and 54703–54704 or for HEGRA observations represented by Aharonian et al (2005); thus, they are excluded [182, 183].

RGB 0136+391: There is only one observation at the VHE gamma-ray band reported in literature and no significant flux variability was detected during that time window: the single observation is marked as a high state.

RGB 0214+517: The source, also known as TXS 0210+515, was observed for over 12 years in the optical band and no significant variability was found. Therefore it is discarded by the second criteria [84].

RGB 0710+591: The source, also known as RGB J0710+591, did not show significant optical variability so it is excluded by the second criteria.

RGB 0847+115: The source, also known as RBS 0723, has just one VHE observation reported and it does not show any significant flux variability; thus, the single observation was marked as a high state.

RGB 1136+676: The source, also known as RX J1136.5+6737, has just one

reported observation at the VHE gamma-ray band; thus, it is marked as a high state.

S2 0109+22: The source has just one reported observation at the VHE gamma-ray band; thus, it is marked as a high state.

S4 0954+65: The source has just one reported observation at the VHE gamma-ray band. The one detection is from single night while the other observations on the nights before and after were non-detections. The single observation is marked as a high state.

S5 0716+714: There are five observations at the VHE gamma-ray band reported in literature from which the low state on MJD 54406–54420 was not used for VHE-optical comparison but only for the VHE-VHE flux comparison due to the third criteria [144]. The other four are clearly high flux states, some of which seem to have a duration of one night only.

TXS 0506+056: There are 7 observations at the VHE gamma-ray band reported in literature. VHE windows on MJD 58020–58028, 58031–58056, 58058–58059 and 58019–58155 are low states but they are excluded by the fourth criteria.

TXS 1515-273: The source has just one reported observation at the VHE gamma-ray band; thus, it is marked as a high state.

VER 0521+211: For the source, also known as VER J0521+211, there are five observations at the VHE gamma-ray band reported in literature. Observations by Prokoph et al. (2015) were done during intermediate flux states of the source and are excluded. Flares on MJD 56625 and 56628 are used as a single high state for the VHE-optical comparison. We could not find any optical data for the observation period presented by Archambault et al. (2013) so the window is discarded [184].

VER 0648+151: For the source, also known as RX J0648.7+1516, there is only one observation at the VHE gamma-ray band by VERITAS. They reported the source to have VHE flux of 3.3% Crab above 200 GeV or 2% Crab above 300 GeV

but no significant flux variability. Thus the single observation is marked as a high state.

PG 1553+113: VHE data for this source was taken from the long term MAGIC light curve compiled by Elisa Prandini (priv. comm.). Intermediate states are excluded: everything from around $3 * 10^{-11}$ cm^{-2} s^{-1} to $5.5 * 10^{-11}$ cm^{-2} s^{-1} above 150 GeV. VERITAS observations represented by Aliu et al. (2015) are all excluded: the first two because they were intermediate states and the last window MJD 56000–56105 is excluded due to the fourth criteria [185]. The MAGIC observations reported by Aleksic et al. (2010) are all intermediate states thus they were discarded as well [186]. Abdalla et al. (2017) reported a non detection of the source by H.E.S.S. that was also discarded due to the third criteria [137]. VERITAS long term observations reported by Gueta (2019) were not included because of the fourth criteria [187]. VHE observation window on MJD 57048–57048 is excluded because we did not find any optical data for that period [157].

Mkn 421: There was a long observation campaign in the VHE gamma-ray band, and the VHE data can be found here [158]. Flares on MJD 56320–56328, 56696–56698, 58183–58199 and 58199–58201 are low significance detections [57] and thus discarded. Also criteria 4 is used here to exclude a few of the flares (variability shorter than 14 weeks), and the intermediate states (MJD 56330–56370, 56399–56695, 57389–57505 and 58138–58225) are also removed. The observation windows are seen in Table 7.

Mkn 501: VHE data for this source was taken from the long term light curve that consist of MAGIC, VERITAS, CAT, Whipple and HEGRA data and was put together by Lea Hackmann (priv. comm.). The light curve is from MJD 50489 to 59083. We only use the VHE data for which we had optical data for which is from MJD 52529 to 59347. The observation windows can be seen in Table 8.

3.4 VHE and optical comparison

To compare the optical state to VHE state systematically, we calculated the average optical flux in each VHE gamma-ray window and compared it to the average optical flux of the source. For instances where the VHE window is shorter than two weeks the optical flux was calculated from ±7 days off the middle point of the VHE window.

Some of the observation windows required more optical data than we had from the Tuorla program so we searched multiple sources for additional data (see section 2.1.1. for details). For some of the sources we could not find optical data so those VHE windows were discarded. Figures 13-14 show the optical light curves of 1ES 1959+650 and B2 1811+31, respectively, along with the VHE observation windows. For 1ES 1959+650 we had very good light curve from the KVA data and did not need to combine it with others, as opposed to B2 1811+31, for which we were missing quite a lot of optical data. The additional data clearly makes the light curve look more whole and is necessary for the VHE data comparison since KVA data does not cover the VHE window. The flux is in Janskys and the date is in Julian days. Red lines are the high states and blue lines correspond to the low states. Each line represent the start of a VHE observation just to make it easier to differentiate each window from another.

We then counted the cases where VHE high state has optical flux above the average optical flux of the whole light curve. In the case of high windows there are 59 where the optical flux is above and 25 where the flux is below the optical average. This is demonstrated in Figure 15. For low windows, there are only 24 where the optical flux is above and 32 where the flux is below the optical average. This is demonstrated in Figure 16. This seems to indicate that high VHE and optical states and low VHE and optical states would go hand in hand.

To check the chance probability of this result we used simulated optical light curves. Elina Lindfors simulated a light curve as red noise light curve with power

spectral density slope similar to values that were determined in Nilsson et al. (2018) for these sources [59]. Almost all sources were consistent with slope -1.5. Lindfors used that value if the source was not in our sample. For blazars OJ287, ON325 and BL Lac a value of -1.3 was used and for blazars 1ES0647+250 and 1ES0806+524 a value of -1.8 was used. After this the simulated light curve was sampled with the observed one as we wanted the sampled-simulated light curve to have observations with exactly the same dates as the observed one. With the same dates I could use them directly to calculate the flux in the VHE window for each 1000 light curves that were produced per source.

This set of simulated light curves allowed me to repeat 1000 the analysis I did for the real data and see in how many of these repetitions I get the same number (or higher) of higher than average optical fluxes in high VHE sample as well as low for the low sample. For the high VHE sample there were only two repetitions out of the 1000 but for the low VHE sample the number was 786. For the high state sample we see that only 0.2% of the simulations the result has very low chance probability and what we see in real data is significant. On the other hand, from the low state sample we see that the chance probability is high and the result from the real data is not significant.

This connection should be analysed further and different methods could be used to calculate the optical flares instead of the Bayesian method. However, the main caveat of VHE-optical comparison analysis is the VHE data. The sample of VHE sources for which we have high and low states well determined is rather small, and we have 17 sources for which we have only one observation marked as a high state. These single observations are often triggered by high state in other bands and therefore could bias our result.

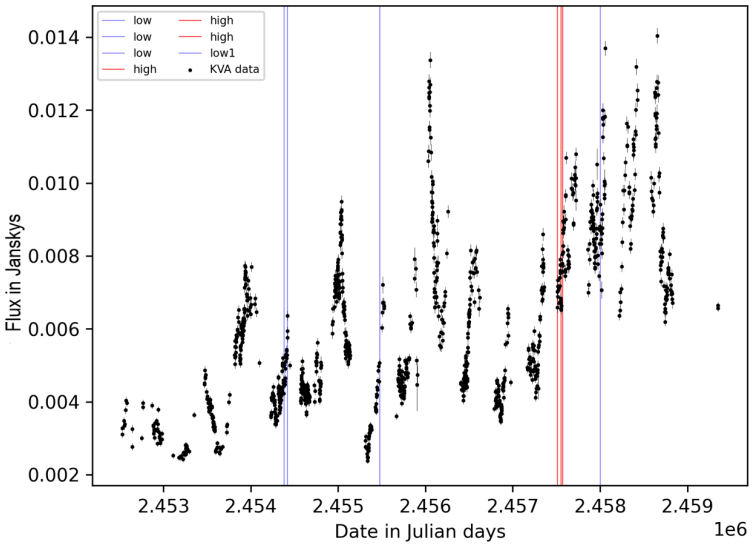

Figure 13: Light curve of the blazar 1ES 1959+650 plotted together with the VHE windows. The flux is in Janskys and the date is in Julian days. Red lines are the high states and blue lines correspond to the low states. Each line represent the start of a VHE observation. There are 7 VHE observation windows, of which 3 are high states that are observed close together but all of them seem to coincide with an optical flare.

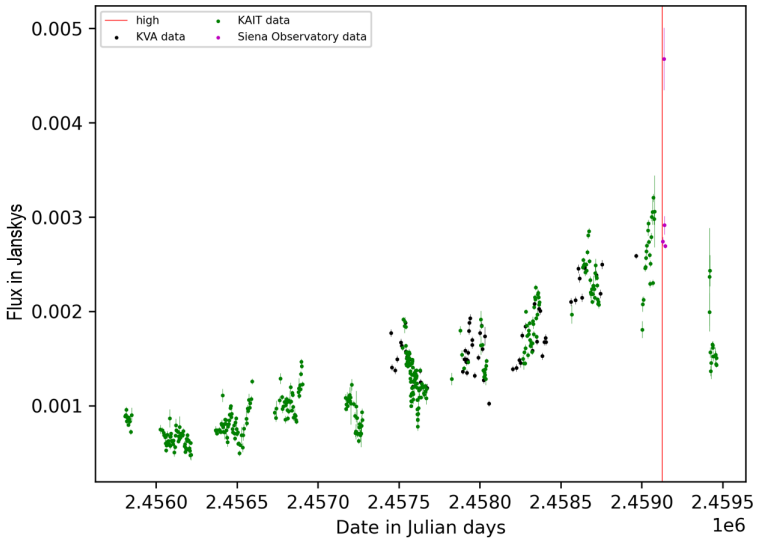

Figure 14: Light curve of the blazar B2 1811+31 plotted together with the VHE window. The flux is in Janskys and the date is in Julian days. Black points are KVA data, green points are KAIT data and magenta points are Siena Observatory data. Red vertical line is the high VHE flux state and the line represents the start of a VHE observation. The VHE detection happened during the optical flare, but as this is the only observation of the source at VHE gamma-rays, it is not certain that it represents VHE high state of the source.

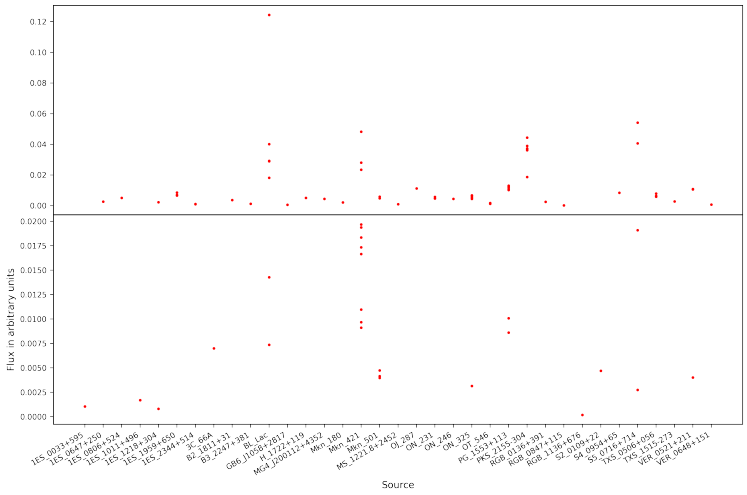

Figure 15: Plot to demonstrate if the average flux of the optical light curve is higher or lower than the average optical flux within each high VHE window for each source. The horizontal line in the middle represents the average optical flux in arbitrary units. If the optical flux in the VHE high state window was higher than the average flux, it is plotted as a circle above this horizontal line and if lower, below the line. There were 59 windows where the flux was higher than the optical average and 25 windows where the flux was lower than the optical average.

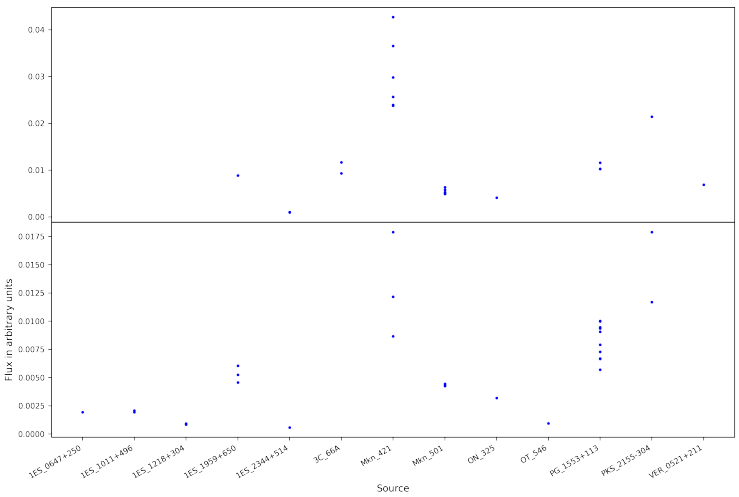

Figure 16: Plot to demonstrate if the average flux of the optical light curve is higher or lower than the average optical flux within each low VHE window for each source. The horizontal line in the middle represents the average optical flux in arbitrary units. If the optical flux in the VHE high state window was higher than the average flux, it is plotted as a circle above this horizontal line and if lower, below the line. There were 24 windows where the flux was higher than the optical average and 32 windows where the flux was lower than the optical average.

4 Results and discussion

I investigated the connection between optical and VHE flares to uncover a common origin for what's causing the flaring in both bands. For this I used a statistical method called Bayesian blocks along with hill-climbing algorithm to first determine the optical flares from the light curves. After this it was important to find out if these flares have a common duration for the comparison with the VHE data since we needed to contain the observations with some kind of criteria. This was due to there being vast amount of different VHE observations with different durations in our sample. We did not find anything conclusive but the results leaned towards two weeks or 14 days.

After this was done, it was time to find the VHE observations that obey our criteria so that we can use them in our study. This was not an easy task, however, due to VHE light curves existing for very few objects and many objects having only one observation. To find a connection we checked how well the high states coincide within the two bands. We wanted to know if the optical and VHE flares overlapped. So I calculated the average optical fluxes for each light curve and within each VHE observation window. We found that on average the optical flux within high VHE flux state epochs is higher than the average optical flux. This result was interesting to be investigated further, and by simulating light curves we wanted to find out the chance probability of this occurring in a repetition of simulated data. The result from this was that for the high state sample the chance probability is very low but for the low state sample, on the other hand, it is high.

Many of the VHE observations of blazars are triggered by high optical states through Target of Opportunity (ToO) observations [188]. This triggered the first systematic analysis of the connection to begin with but also causes clear bias to our sample. In particular, the observations of many sources, which only have a single detection we considered as high state, have been ToO observations due to high state

in other wavebands.

Optical emission is synchrotron emission, while VHE gamma-rays are inverse Compton emission, either SSC or EC. The SSC and EC mechanisms both predict a connection between optical and gamma-ray flares and several mechanisms may affect the time-lags between optical and gamma-ray flares but their relative order is impossible to predict [188]. Optical to VHE gamma-ray connection should also be affected by the synchrotron peak frequency of the source since higher peak frequency in the X-ray band leads to the variability in the optical domain to be in some cases very small and the synchrotron flares have the best visibility in the X-ray range as is apparent for blazars Mrk 421 and Mrk 501.

The findings of this thesis are in line with previous studies with much smaller samples. For example, in Lindfors et al. (2009), systematic comparison was possible only for 7 sources, 6 of which seemed to show high state simultaneously in optical and VHE gamma-ray bands. Even if the sample of this thesis is significantly larger, 36 sources, further observations in VHE gamma-ray band are needed to remove the observational biases from our sample. Furthermore, real correlation studies between optical and VHE gamma-ray band would be needed, as more VHE gamma-ray light curves will become available.

Acknowledgements

I would like to thank Dr. Vandad Fallah Ramazani for his help and supervision in recovering and collecting the VHE gamma-ray data.

References

[1] D. Lynden-Bell, Nature **223**, 690 (1969).

[2] N. I. Shakura and R. A. Sunyaev, Astronomy & Astrophysics **24**, 337 (1973).

[3] R. Chatterjee *et al.*, The Astrophysical Journal **689**, 79 (2008).

[4] A. P. Marscher *et al.*, Nature **452**, 966 (2008).

[5] A. P. Marscher *et al.*, Astrophysical Journal Letters **710**, 126 (2010).

[6] S. G. Jorstad *et al.*, Astrophysical Journal **715**, 362 (2010).

[7] M. L. Ahnen *et al.*, Astronomy and Astrophysics **593**, 91 (2016).

[8] R. J. Britto *et al.*, The Astrophysical Journal **830**, 162 (2016).

[9] T. Hovatta *et al.*, Astronomy and Astrophysics **469**, 899 (2007).

[10] J. H. Krolik and T. Di Matteo, American Journal of Physics **68**, 489 (2000).

[11] C. Ricci, Active Galactic Nuclei (AGN) [online, cited 2.6.2022]. Available in www-form <https://www.isdc.unige.ch/∼ricci/Website/Welcome.html>., 2013.

[12] S. Kaspi *et al.*, The Astrophysical Journal **629**, 61 (2005).

[13] C. M. Urry and P. Padovani, Publications of the Astronomical Society of the Pacific **107**, 803 (1995).

[14] M. Suganuma *et al.*, The Astrophysical Journal **639**, 46 (2006).

[15] M. Rowan-Robinson, The Astrophysical Journal **213**, 635 (1977).

[16] A. Lawrence and M. Elvis, The Astrophysical Journal **256**, 410 (1982).

[17] M. Türler *et al.*, Astronomy and Astrophysics Supplement Series **134**, 89 (1999).

[18] R. Scarpa and R. Falomo, Astronomy and Astrophysics **325**, 109 (1997).

[19] P. Giommi, P. Padovani, and G. Polenta, Monthly Notices of the Royal Astronomical Society **431**, 1914 (2013).

[20] B. L. Fanaroff and J. M. Riley, Monthly Notices of the Royal Astronomical Society **167**, 31 (1974).

[21] H. Landt and H. E. Bignall, Monthly Notices of the Royal Astronomical Society **391**, 967 (2008).

[22] P. Kharb, M. L. Lister, and N. J. Cooper, Astrophysical Journal **710**, 764 (2010).

[23] A. A. Abdo *et al.*, Astrophysical Journal **716**, 30 (2010).

[24] E. T. Meyer, G. Fossati, M. Georganopoulos, and M. L. Lister, Astrophysical Journal **740**, 98 (2011).

[25] R. C. Vermeulen *et al.*, The Astrophysical Journal **452**, (1995).

[26] E. A. Corbett, A. Robinson, D. J. Axon, and J. H. Hough, Monthly Notices of the Royal Astronomical Society **311**, 485 (2000).

[27] C. M. Raiteri *et al.*, Astronomy and Astrophysics **464**, 871 (2007).

[28] E. T. Meyer, G. Fossati, M. Georganopoulos, and M. L. Lister, Astrophysical Journal **740**, 98 (2011).

[29] J. H. Beall, in *Proceedings of Science* (Sissa Medialab Srl , 2015), Vol. 2015-May.

[30] A. H. Bridle and R. A. Perley, Annual Review of Astronomy and Astrophysics **22**, 319 (1984).

[31] R. A. Laing, Nature **331**, 149 (1988).

[32] T. Hovatta and E. Lindfors, New Astronomy Reviews **87**, (2019).

[33] A. Lähteenmäki and E. Valtaoja, The Astrophysical Journal **521**, 493 (1999).

[34] M. L. Lister *et al.*, The Astronomical Journal **152**, 12 (2016).

[35] M. J. Rees, Nature **211**, 468 (1966).

[36] R. Laing, C. Jenkins, J. Wall, and S. Unger, in *A.S.P. Conference Series*, edited by G. V. Bicknell, M. A. Dopita, and P. J. Quinn (Astronomical Society of the Pacific , 1994), Vol. 54, p. 201.

[37] D. S. de Young, The Astrophysical Journal **405**, L13 (1993).

[38] A. Tchekhovskoy and O. Bromberg, Monthly Notices of the Royal Astronomical Society: Letters **461**, L46 (2016).

[39] A. P. Marscher and W. K. Gear, The Astrophysical Journal **298**, 114 (1985).

[40] P. A. Hughes, H. D. Aller, and M. F. Aller, The Astrophysical Journal **298**, 301 (1985).

[41] M. Spada, G. Ghisellini, D. Lazzati, and A. Celotti, Monthly Notices of the Royal Astronomical Society **325**, 1559 (2001).

[42] M. Joshi and M. Bottcher, The Astrophysical Journal **662**, 884 (2007).

[43] P. B. Graff, M. Georganopoulos, E. S. Perlman, and D. Kazanas, The Astrophysical Journal **689**, 68 (2008).

[44] H. Zhang, H. Li, F. Guo, and G. Taylor, The Astrophysical Journal **835**, 125 (2017).

[45] J. G. Kirk and P. Duffy, Particle acceleration and relativistic shocks, 1999.

[46] R. Vainio, J. J. Virtanen, and R. Schlickeiser, Astronomy and Astrophysics **409**, 821 (2003).

[47] J. J. P. Virtanen and R. Vainio, The Astrophysical Journal **621**, 313 (2005).

[48] E. Angelakis *et al.*, Monthly Notices of the Royal Astronomical Society **463**, 3365 (2016).

[49] D. Giannios and H. Spruit, Astronomy & Astrophysics **450**, 887 (2006).

[50] L. Sironi, M. Petropoulou, and D. Giannios, Monthly Notices of the Royal Astronomical Society **450**, 183 (2015).

[51] I. M. Christie, M. Petropoulou, L. Sironi, and D. Giannios, Monthly Notices of the Royal Astronomical Society **482**, 65 (2019).

[52] M. Petropoulou, D. Giannios, and L. Sironi, Monthly Notices of the Royal Astronomical Society **462**, 3325 (2016).

[53] C. Hoffmeister, Astronomische Nachrichten **236**, 233 (1929).

[54] P. A. Strittmatter *et al.*, The Astrophysical Journal **175**, L7 (1972).

[55] R. Falomo, E. Pian, and A. Treves, An optical view of BL Lacertae objects, 2014.

[56] R. Chatterjee *et al.*, Astrophysical Journal **749**, 191 (2012).

[57] A. Arbet-Engels *et al.*, Astronomy and Astrophysics **647**, (2021).

[58] Tuorla Observatory blazar monitoring program [online, cited 24.1.2022]. Available in www-form <https://users.utu.fi/kani/1m/>.

[59] K. Nilsson *et al.*, Astronomy and Astrophysics **620**, 185 (2018).

[60] K. Nilsson *et al.*, Astronomy and Astrophysics **475**, 199 (2007).

[61] W. Zheng, The Katzman Automatic Imaging Telescope [online, cited 20.2.2022]. Available in www-form <https://w.astro.berkeley.edu/bait/kait.html>., 2016.

[62] Zwicky Transient Facility [online, cited 10.2.2022]. Available in www-form <https://www.ipac.caltech.edu/project/ztf>., 2017.

[63] Italian Supernovae Search Project [online, cited 10.2.2022]. Available in www-form <http://italiansupernovae.org/en/project/description.html>.

[64] Department of Astronomy and Steward Observatory [online, cited 10.2.2022]. Available in www-form <https://www.as.arizona.edu/>.

[65] Catalina Real-Time Transient Survey [online, cited 10.2.2022]. Available in www-form <http://crts.caltech.edu/>.

[66] Galayda, MDM Observatory [online, cited 10.2.2022]. Available in www-form <http://mdm.kpno.noirlab.edu/>., 2022.

[67] E. Aliu *et al.*, Astrophysical Journal **742**, 127 (2011).

[68] Georgian National Astrophysical Observatory [online, cited 1.5.2022]. Available in www-form <http://www.genao.org/>.

[69] Burke-Gaffney Observatory [online, cited 1.5.2022]. Available in www-form <https://www.smu.ca/astronomy-physics/burke-gaffney-observatory.html>.

[70] Crimean Astrophysical Observatory [online, cited 1.5.2022]. Available in www-form <https://crao.ru/en/about-en/svedenia-en>.

[71] Wikipedia. Lulin Observatory [online, cited 1.5.2022]. Available in www-form <https://en.wikipedia.org/wiki/Lulin_Observatory>.

[72] Las Cumbres Observatory [online, cited 1.5.2022]. Available in www-form <https://lco.global/observatory/telescopes/0m4/>.

[73] Perkins Observatory [online, cited 1.5.2022]. Available in www-form <https://www.owu.edu/about/offices-services-directory/perkins-observatory/>.

[74] Wikipedia. Rozhen Observatory [online, cited 1.5.2022]. Available in www-form <https://en.wikipedia.org/wiki/Rozhen_Observatory>.

[75] Pulkovo Observatory [online, cited 1.5.2022]. Available in www-form <http://www.gaoran.ru/english/>.

[76] Instituto de Astrofisica de Canarías. Observatorios de Canarías. IAC80 Telescope [online, cited 1.5.2022]. Available in www-form <http://research.iac.es/OOCC/iac-managed-telescopes/iac80/>.

[77] Gravitational wave Optical Transient Observatory [online, cited 1.5.2022]. Available in www-form <https://www.iac.es/en/observatorios-de-canarias/telescopes-and-experiments/gravitational-wave-optical-transient-observatory>.

[78] J. D. Scargle, The Astrophysical Journal **504**, 405 (1998).

[79] J. D. Scargle, J. P. Norris, B. Jackson, and J. Chiang, Astrophysical Journal **764**, 167 (2013).

[80] Jormanainen Jenni, Master's thesis, University of Turku, 2019.

[81] How CTAO Works [online, cited 10.4.2023]. Available in www-form <https://www.cta-observatory.org/about/how-cta-works/>., 2016.

[82] S. Wakely and H. Deirdre, TeVCat [online, cited 10.2.2022]. Available in www-form <http://tevcat.uchicago.edu/>.

[83] V. F. Ramazani, E. Lindfors, and K. Nilsson, Astronomy and Astrophysics **608**, 68 (2017).

[84] E. J. Lindfors *et al.*, Astronomy and Astrophysics **593**, (2016).

[85] H. Ku, Journal of Research of the National Bureau of Standards, Section C: Engineering and Instrumentation **70C**, 263 (1966).

[86] J. Aleksić *et al.*, Astroparticle Physics **72**, 76 (2016).

[87] J. Aleksic *et al.*, Monthly Notices of the Royal Astronomical Society **446**, 217 (2015).

[88] P. Cogan, in *Proceedings of the 30th International Cosmic Ray Conference, ICRC 2007*, edited by J. F. V.-G. R. Caballero, J. C. D'Olivo, G. Medina-Tanco, L. Nellen, F. A. Sánchez (International Union of Pure and Applied Physics , 2007), Vol. 3, pp. 921–924.

[89] R. Mirzoyan, Detection of sub-TeV gamma-ray emission from the flaring blazar TXS 1515-273 with the MAGIC telescopes [online, cited 28.2.2022]. Available in www-form <https://www.astronomerstelegram.org/?read=12538>., 2019.

[90] J. Aleksić *et al.*, Monthly Notices of the Royal Astronomical Society **451**, 739 (2015).

[91] J. Aleksić *et al.*, Astronomy and Astrophysics **591**, (2016).

[92] R. Mirzoyan, Exceptionally high >100 GeV flux state of 1ES 1011+496 [online, cited 28.2.2022]. Available in www-form <https://www.astronomerstelegram.org/?read=5887>., 2014.

[93] M. L. Ahnen *et al.*, Astronomy and Astrophysics **590**, (2016).

[94] V. A. Acciari *et al.*, Astrophysical Journal **695**, 1370 (2009).

[95] V. A. Acciari *et al.*, Astrophysical Journal Letters **709**, 163 (2010).

[96] S. O'Brien, in *Proceedings of Science* (Sissa Medialab Srl , 2019), Vol. 358.

[97] E. Aliu *et al.*, Astrophysical Journal **779**, (2013).

[98] V. A. Acciari *et al.*, Broadband characterisation of the very intense TeV flares of the blazar 1ES 1959+650 in 2016, 2020.

[99] A. Biland, FACT measures new maximum flux from the HBL 1ES 1959+650 at TeV energies [online, cited 28.2.2022]. Available in www-form <https://www.astronomerstelegram.org/?read=9239>., 2016.

[100] S. Buson *et al.*, Fermi-LAT, FACT, MAGIC and VERITAS detection of increasing gamma-ray activity from the high-energy peaked BL Lac object 1ES 1959+650 [online, cited 28.2.2022]. Available in www-form <https://www.astronomerstelegram.org/?read=9010>., 2016.

[101] S. Sakurai *et al.*, in *Proceedings of Science* (Sissa Medialab Srl , 2021).

[102] J. Albert *et al.*, The Astrophysical Journal **662**, 892 (2007).

[103] V. A. Acciari *et al.*, Astrophysical Journal **738**, 169 (2011).

[104] J. Aleksić *et al.*, Astronomy and Astrophysics **556**, (2013).

[105] C. Allen *et al.*, Monthly Notices of the Royal Astronomical Society **471**, 2117 (2017).

[106] V. A. Acciari *et al.*, Astronomy and Astrophysics **640**, (2020).

[107] V. A. Acciari *et al.*, Monthly Notices of the Royal Astronomical Society **496**, 3912 (2020).

[108] A. Furniss, in *2014 Fermi Symposium proceedings*, edited by R. I. Yasushi Fukazawa, Yasuyuki Tanaka (NASA's HEASARC , 2014).

[109] J. Aleksić *et al.*, Astrophysical Journal **726**, 58 (2011).

[110] O. Blanch, Detection of very-high-energy gamma-ray emission from B2 1811+31 with the MAGIC telescopes [online, cited 28.2.2022]. Available in www-form <https://www.astronomerstelegram.org/?read=14090>., 2020.

[111] J. Aleksić *et al.*, Astronomy and Astrophysics **539**, 31 (2012).

[112] J. Albert *et al.*, The Astrophysical Journal **666**, L17 (2007).

[113] T. Arlen *et al.*, Astrophysical Journal **762**, 92 (2013).

[114] V. A. Acciari *et al.*, Astronomy and Astrophysics **623**, (2019).

[115] Q. Feng *et al.*, in *Proceedings of Science* (Sissa Medialab Srl , 2017).

[116] R. Mirzoyan, MAGIC detection of an increased activity from BL Lacertae at very-high-energy gamma rays [online, cited 28.2.2022]. Available in www-form <https://www.astronomerstelegram.org/?read=12724>., 2019.

[117] O. Blanch, Detection of flaring very-high-energy gamma-ray emission from BL Lacertae with the MAGIC telescopes [online, cited 28.2.2022]. Available in www-form <https://www.astronomerstelegram.org/?read=14826>., 2021.

[118] O. Blanch, etection of very-high-energy gamma-ray emission from GB6 J1058+2817 with the MAGIC telescopes [online, cited 28.2.2022]. Available in www-form <https://www.astronomerstelegram.org/?read=14506>., 2021.

[119] M. L. Ahnen *et al.*, Monthly Notices of the Royal Astronomical Society **459**, 3271 (2016).

[120] J. Aleksić *et al.*, Astronomy and Astrophysics **572**, 40 (2014).

[121] J. Albert *et al.*, The Astrophysical Journal **648**, L105 (2006).

[122] J. Cortina, Discovery of Very High Energy Gamma-Ray Emission from MS1221.8+2452 with the MAGIC telescopes [online, cited 28.2.2022]. Available in www-form <https://www.astronomerstelegram.org/?read=5038>., 2013.

[123] S. O'Brien, in *Proceedings of Science* (Sissa Medialab Srl , 2017).

[124] V. A. Acciari *et al.*, The Astrophysical Journal **684**, L73 (2008).

[125] V. A. Acciari *et al.*, Astrophysical Journal **707**, 612 (2009).

[126] J. Vievering, in *Proceedings of Science* (Sissa Medialab Srl , 2015), Vol. 30-July-20.

[127] W. Benbow, in *Proceedings of Science* (Sissa Medialab Srl , 2017).

[128] J. Aleksić *et al.*, Astronomy and Astrophysics **544**, 36 (2012).

[129] M. Mariotti, Discovery of Very High Energy Gamma-Ray Emission from 1ES 1215+303 by MAGIC [online, cited 28.2.2022]. Available in www-form <https://www.astronomerstelegram.org/?read=3100>., 2011.

[130] A. U. Abeysekara *et al.*, The Astrophysical Journal **836**, 205 (2017).

[131] J. Valverde *et al.*, The Astrophysical Journal **891**, 170 (2020).

[132] M. Mariotti, MAGIC discovers VHE gamma-ray emission from the blazar 1ES 1727+502 [online, cited 28.2.2022]. Available in www-form <https://www.astronomerstelegram.org/?read=3774>., 2011.

[133] S. Archambault *et al.*, Astrophysical Journal **808**, 110 (2015).

[134] Y. Sakamoto *et al.*, The Astrophysical Journal **676**, 113 (2008).

[135] H. Abdalla *et al.*, Astronomy and Astrophysics **598**, 39 (2017).

[136] Online material related to the H.E.S.S. data publishe [online, cited 28.2.2022]. Available in www-form <https://www.mpi-hd.mpg.de/hfm/HESS/pages/publications/auxiliary/auxinfo_PKS2155_2004_2012.htm 2017.

[137] H. Abdalla *et al.*, Astronomy and Astrophysics **600**, 55 (2017).

[138] A. Wierzcholska, M. Zacharias, F. Jankowsky, and S. Wagner, Galaxies **7**, (2019).

[139] M. collaboration (unpublished).

[140] R. Mirzoyan, DISCOVERY OF VERY HIGH ENERGY GAMMA-RAY EMISSION FROM RBS 0723 WITH THE MAGIC TELESCOPES [online, cited 28.2.2022]. Available in www-form <https://www.astronomerstelegram.org/?read=5768>., 2014.

[141] R. Mirzoyan, Discovery of Very High Energy Gamma-Ray Emission from BL Lac object RX J1136.5+6737 by the MAGIC Telescopes [online, cited 28.2.2022]. Available in www-form <https://www.astronomerstelegram.org/?read=6062>., 2014.

[142] S. Ansoldi *et al.*, Monthly Notices of the Royal Astronomical Society **480**, 879 (2018).

[143] M. L. Ahnen *et al.*, Astronomy and Astrophysics **617**, 44 (2018).

[144] D. Mazin *et al.*, in *Proceedings of the 31st International Cosmic Ray Conference, ICRC 2009* (Sissa Medialab Srl , 2009), pp. 714–717.

[145] M. L. Ahnen *et al.*, Astronomy and Astrophysics **619**, (2018).

[146] R. Mirzoyan, MAGIC detection of an unprecedented activity from S50716+714 at very-high-energy gamma rays [online, cited 16.3.2022]. Available in www-form <https://www.astronomerstelegram.org/?read=11100>., 2017.

[147] S. Ansoldi *et al.*, The Astrophysical Journal **863**, L10 (2018).

[148] A. U. Abeysekara *et al.*, The Astrophysical Journal **861**, L20 (2018).

[149] R. Mirzoyan, MAGIC detects enhanced flux of VHE gamma rays from TXS 0506+056 [online, cited 28.2.2022]. Available in www-form <https://www.astronomerstelegram.org/?read=12260>., 2018.

[150] V. A. Acciari *et al.*, Monthly Notices of the Royal Astronomical Society **507**, 1528 (2021).

[151] H. Prokoph, P. Da Vela, and C. Schultz, in *Proceedings of Science* (Sissa Medialab Srl , 2015), Vol. 30-July-20.

[152] J. Quinn, VERITAS detection of unprecedented gamma-ray flare from the blazar VER J0521+211 [online, cited 28.2.2022]. Available in www-form <https://www.astronomerstelegram.org/?read=13522>., 2020.

[153] E. Aliu *et al.*, Astrophysical Journal **742**, 127 (2011).

[154] F. Aharonian *et al.*, Astronomy and Astrophysics **477**, 481 (2008).

[155] O. Blanch, MAGIC detection of an increased activity from PG 1553+113 in very-high-energy gamma rays [online, cited 16.3.2022]. Available in www-form <https://www.astronomerstelegram.org/?read=14520>., 2021.

[156] A. Abramowski *et al.*, Astrophysical Journal **802**, 65 (2015).

[157] E. Prandini (unpublished).

[158] VizieR [online, cited 10.2.2022]. Available in www-form <https://vizier.cds.unistra.fr/viz-bin/VizieR>., 1996.

[159] A. Abramowski *et al.*, Astronomy and Astrophysics **538**, 103 (2012).

[160] E. Aliu *et al.*, Astrophysical Journal **755**, 118 (2012).

[161] R. A. Ong, Discovery of VHE Gamma-Ray Emission from the Fermi-LAT Source 1ES 0502+675 [online, cited 28.2.2022]. Available in www-form <https://www.astronomerstelegram.org/?read=2301>., 2009.

[162] W. Benbow, in *Proceedings of the 32nd International Cosmic Ray Conference, ICRC 2011* (Sissa Medialab Srl , 2011), Vol. 8, pp. 51–54.

[163] J. Dumm, in *Proceedings of the 33rd International Cosmic Rays Conference, ICRC 2013* (Sissa Medialab Srl , 2013), Vol. 2013-Octob.

[164] F. Aharonian *et al.*, Astronomy and Astrophysics **421**, 529 (2004).

[165] K. Berger *et al.*, in *Proceedings of the 33rd International Cosmic Rays Conference, ICRC 2013* (Sissa Medialab Srl , 2013).

[166] M. Mariotti, MAGIC observes a very high energy gamma-ray flare from 1ES0806+524 [online, cited 28.2.2022]. Available in www-form <https://www.astronomerstelegram.org/?read=3192>., 2011.

[167] J. Albert *et al.*, The Astrophysical Journal **667**, 21 (2007).

[168] J. Albert *et al.*, Monthly Notices of the Royal Astronomical Society **642**, 202 (2006).

[169] S. Lombardi *et al.*, in *Proceedings of the 32nd International Cosmic Ray Conference, ICRC 2011* (Sissa Medialab Srl , 2011), Vol. 8, pp. 151–154.

[170] K. K. Singh *et al.*, New Astronomy **36**, 1 (2015).

[171] M. Santander, in *Proceedings of Science* (Sissa Medialab Srl , 2017).

[172] F. Aharonian *et al.*, Astronomy and Astrophysics **406**, 9 (2003).

[173] H. Krawczynski *et al.*, The Astrophysical Journal **601**, 151 (2004).

[174] M. Catanese *et al.*, The Astrophysical Journal **501**, 616 (1998).

[175] A. Konopelko and J. Kettler, in *HEGRA Collaboration* (American Institute of Physics Heilderberg, 1999).

[176] W. Zheng, A. V. Filippenko, and R. W. Romani, KAIT Fermi AGN Light-Curve Reservoir [online, cited 10.2.2022]. Available in www-form <http://herculesii.astro.berkeley.edu/kait/agn/lightcurve_all/>., 2019.

[177] O. Blanch, Detection of a bright very-high-energy gamma-ray flare from BL Lac with the MAGIC telescopes [online, cited 28.2.2022]. Available in www-form <https://www.astronomerstelegram.org/?read=14032>., 2020.

[178] R. Mukherjee, VERITAS Detection of VHE Emission from OJ 287 [online, cited 10.2.2022]. Available in www-form <https://www.astronomerstelegram.org/?read=10051>., 2017.

[179] J. Aleksić *et al.*, Astronomy and Astrophysics **544**, 75 (2012).

[180] F. Aharonian *et al.*, Astronomy and Astrophysics **502**, 749 (2009).

[181] F. Aharonian *et al.*, The Astrophysical Journal **664**, L71 (2007).

[182] F. Aharonian *et al.*, Astronomy and Astrophysics **442**, 895 (2005).

[183] F. Aharonian *et al.*, Astronomy and Astrophysics **430**, 865 (2005).

[184] S. Archambault *et al.*, Astrophysical Journal **776**, (2013).

[185] E. Aliu *et al.*, Astrophysical Journal **799**, (2015).

[186] J. Aleksíc *et al.*, Astronomy and Astrophysics **515**, 76 (2010).

[187] O. Gueta, in *Proceedings of Science* (Sissa Medialab Srl , 2019), Vol. 358.

[188] E. J. Lindfors *et al.*, in *Proceedings of the 31st International Cosmic Ray Conference, ICRC 2009* (Sissa Medialab Srl , 2009).